The Astrophysical Journal, 779:79 (22pp), 2013 December 10 doi:10.1088/0004-637X/779/1/79
© 2013. The American Astronomical Society. All rights reserved. Printed in the U.S.A.

THE GALACTIC CENSUS OF HIGH- AND MEDIUM-MASS PROTOSTARS. II. LUMINOSITIES AND EVOLUTIONARY STATES OF A COMPLETE SAMPLE OF DENSE GAS CLUMPS

Bo Ma[1], Jonathan C. Tan[1,2], and Peter J. Barnes[1]
[1] Department of Astronomy, University of Florida, FL 32611, USA
[2] Department of Physics, University of Florida, FL 32611, USA
Received 2012 November 27; accepted 2013 September 20; published 2013 November 26

ABSTRACT

The Census of High- and Medium-mass Protostars (CHaMP) is the first large-scale ($280^\circ < l < 300^\circ$, $-4^\circ < b < 2^\circ$), unbiased, subparsec resolution survey of Galactic molecular clumps and their embedded stars. Barnes et al. presented the source catalog of ∼300 clumps based on HCO^+(1–0) emission, used to estimate masses M. Here we use archival midinfrared-to-millimeter continuum data to construct spectral energy distributions. Fitting two-temperature gray-body models, we derive bolometric luminosities, L. We find that the clumps have $10 \lesssim L/L_\odot \lesssim 10^{6.5}$ and $0.1 \lesssim L/M/[L_\odot/M_\odot] \lesssim 10^3$, consistent with a clump population spanning a range of instantaneous star-formation efficiencies from 0 to ∼50%. We thus expect L/M to be a useful, strongly varying indicator of clump evolution during the star cluster formation process. We find correlations of the ratio of warm-to-cold component fluxes and of cold component temperature with L/M. We also find a near-linear relation between L/M and *Spitzer*-IRAC specific intensity (surface brightness); thus, this relation may also be useful as a star-formation efficiency indicator. The lower bound of the clump L/M distribution suggests that the star-formation efficiency per free-fall time is $\epsilon_{\rm ff} < 0.2$. We do not find strong correlations of L/M with mass surface density, velocity dispersion, or virial parameter. We find a linear relation between L and $L_{\rm HCO^+(1-0)}$, although with large scatter for any given individual clump. Fitting together with extragalactic systems, the linear relation still holds, extending over 10 orders of magnitude in luminosity. The complete nature of the CHaMP survey over a several kiloparsec-scale region allows us to derive a measurement at an intermediate scale, bridging those of individual clumps and whole galaxies.

Key words: dust, extinction – stars: formation – stars: pre-main sequence – surveys

Online-only material: color figures, machine-readable tables

1. INTRODUCTION

Stars form from the gravitational collapse of the densest regions of giant molecular clouds (GMCs). In particular, star clusters, likely the dominant mode of star formation (Lada & Lada 2003; Gutermuth et al. 2009), are born from ∼ parsec-scale gas *clumps* within GMCs. However, many open questions remain (see, e.g., McKee & Ostriker 2007; Tan et al. 2013; Hennebelle & Falgarone 2012). How are GMCs formed out of the diffuse interstellar medium? Why does star formation occur in only a small fraction of the available gas in GMCs? What is the star formation rate (SFR) and efficiency over the GMC lifetime and what processes control this? What is the timescale of star cluster formation: is it fast (Elmegreen 2000, 2007) or slow (Tan et al. 2006) with respect to the free-fall time? What processes control the evolution and overall star formation efficiency of a star-forming clump?

To help address some of these open questions, Barnes et al. (2011, hereafter Paper I) have designed a multiwavelength survey, the Census of High- and Medium-mass Protostars (CHaMP). Starting in the 3 mm band, the aim of CHaMP has been to map a complete sample of molecular gas structures in a $20^\circ \times 6^\circ$ region in the Galactic plane ($280^\circ < l < 300^\circ$, $-4^\circ < b < +2^\circ$) and to measure their associated star formation activity from the near-to-far-IR. Using the 4 m Nanten telescope, this region was first surveyed in the $J = 1$–0 transitions of ^{12}CO, ^{13}CO, C^{18}O, and HCO^+ (Yonekura et al. 2005). This sequence of species traces progressively higher densities, and the mapping was carried out in this order so as to identify all the locations of dense gas without having to map the entire region in the tracers of the densest gas. Thus ^{13}CO was only observed where the ^{12}CO integrated intensity was above 10 K km s^{-1}, and C^{18}O and HCO^+ were observed where ^{13}CO was brighter than 5 K km s^{-1}. Then a follow-up campaign was begun to map the dense gas regions found in the Nanten survey. The follow-up is conducted in a number of 3 mm molecular transitions with the 22 m Mopra telescope at a much higher sensitivity and angular resolution than the Nanten telescope (Paper I). This observing strategy distinguishes the CHaMP survey from all other Galactic plane surveys of dense gas.

In Paper I, maps of the CHaMP regions in HCO^+(1–0) line emission observed by the Mopra telescope were presented. A total of 303 massive molecular clumps were identified. This sample has the following properties: integrated line intensities 1–30 K km s^{-1}, linewidths 1–9 km s^{-1}, FWHM sizes 0.2–2 pc, mean mass surface densities $\Sigma \sim 0.01$ to ∼1 g cm^{-2}, and masses ∼ 10 to ∼10^4 $M_\odot$.

In this article, we use archival infrared and millimeter data to investigate the spectral energy distributions (SEDs) and luminosities of these HCO^+ clumps, with the goal being to characterize their evolutionary state with respect to star cluster formation. The article is organized as follows. Section 2 describes the IR and millimeter (mm) data used in this study. Section 3 describes our methods of estimating clump fluxes. Section 4 presents our results, including the clump masses, bolometric fluxes, bolometric luminosities, luminosity-to-mass ratios, warm and hot component fluxes, cold component temperatures, and bolometric temperatures. In particular, we examine the correlation of various potential tracers of embedded stellar content with the luminosity-to-mass ratio and then emphasize the use of this ratio

as an evolutionary indicator for star cluster formation. Section 5 presents further discussion, including searches for potential correlation of luminosity-to-mass ratio with clump mass surface density and virial parameter. It also discusses the luminosity versus HCO^+ line luminosity relation from clumps to whole galaxies. Section 6 summarizes our conclusions.

2. INFRARED AND MILLIMETER OBSERVATIONAL DATA

The first goal of this article is to measure fluxes at various wavelengths coming from the CHaMP clumps. Here we describe the main observational data sets that we use to derive these fluxes.

2.1. MSX

The *Midcourse Space Experiment* (*MSX*) was launched in 1996 April. It conducted a Galactic plane survey ($0^\circ < l < 360^\circ$, $|b| < 5^\circ$), which covers all the CHaMP clumps. The four *MSX* band wavelengths are centered at 8.28, 12.13, 14.65, and 21.3 μm. The best image resolution is $\sim 18''$ in the 8.28 μm band, with positional accuracy of about $2''$. The instrumentation and survey are described by Egan & Price (1996). Calibrated images of the Galactic plane were obtained from the online *MSX* image server at the IPAC website at http://irsa.ipac.caltech.edu/data/MSX/. For simplicity, we assume conservative common absolute flux uncertainties of 20% for all the IR data (*MSX*, *IRAS*, *Spitzer* IRAC), similar to that estimated for *Infrared Astronomical Satellite* (*IRAS*; M. Cohen 1999, private communication).

2.2. IRAS

The *IRAS* performed an all-sky survey at 12, 25, 60, and 100 μm. The nominal resolution is about $4'$ at 60 μm. High Resolution Image Restoration (HIRES) uses the maximum correlation method (Aumann et al. 1990) to produce higher resolution images, better than $1'$ at 60 μm. Sources chosen for processing with HIRES were processed at all four *IRAS* bands with 20 iterations. The pixel size was set to $15''$ with a 1° field centered on the target. The absolute fluxes of the *IRAS* data are expected to be accurate to about 20%.

2.3. Spitzer IRAC

The *Spitzer* InfraRed Array Camera (IRAC) is a four-channel camera that provides simultaneous $5\farcm2 \times 5\farcm2$ images at 3.6, 4.5, 5.8, and 8 μm with a pixel size of $1\farcs2 \times 1\farcs2$ and an angular resolution of about $2''$ at 8 μm. We searched the *Spitzer* archive at http://irsa.ipac.caltech.edu/applications/Spitzer/SHA/ for IRAC data near the positions of our HCO^+ clumps. We found IRAC data for 284 out of our 303 clumps. Most of these data are from two large survey programs: PID 189 (Churchwell, E., "The SIRTF Galactic Plane Survey") and PID 40791 (Majewski, S., "Galactic Structure and Star Formation in Vela-Carina"). We used the post-basic calibration data to estimate the fluxes of these clumps, which we assume has a 20% uncertainty.

2.4. Millimeter Data

Hill et al. (2005) carried out a 1.2 mm continuum emission survey toward 131 star-forming complexes using the Swedish ESO Submillimetre Telescope (SEST) IMaging Bolometer Array (SIMBA). SIMBA is a 37 channel hexagonal bolometer array operating at a central frequency of 250 GHz (1.2 mm), with a bandwidth of 50 GHz. It has a half-power beam width of $24''$ for a single element, and the separation between elements on the sky is 44 arcseconds. Hill et al. list the 1.2 mm flux for 404 sources, 15 of which are in our sample.

3. DATA ANALYSIS

3.1. Definition of Clump Angular Area and HCO^+ Masses

Paper I presented maps of the CHaMP region in HCO^+(1–0) line emission using the 22 m Mopra telescope, identifying 303 massive molecular clumps. Elliptical clump sizes were defined based on two-dimensional Gaussian fitting for each HCO^+ clump. The ellipse size quoted in Columns 9 and 10 of Table 4 of Paper I is the FWHM angular size of the major and minor axes of the Gaussian fit. Clump masses, M, were evaluated based on integrating the derived column density distribution over the full area of the Gaussian profile ($M_{\rm col}$ listed in Column 9 of their Table 5). We note that the derivation of mass surface densities and masses from the observed HCO^+(1–0) intensity depends on several factors. (1) In the view of one person on our team (J.C.T.), the conversion of observed HCO^+(1–0) line intensity to total HCO^+ column density is assumed to have an uncertainty of $\sim$30%; in the view of another (P.J.B.), there is no identifiable reason for this assumption, since the analysis in Paper I showed that there is no such uncertainty, beyond the points mentioned next. (2) The abundance of HCO^+ is also significant ($X_{\rm HCO^+} \equiv n_{\rm HCO^+}/n_{\rm H2} = 1.0 \times 10^{-9}$ was adopted in Paper I, being a median value from a number of observational and astrochemical studies). The uncertainty in this mean abundance is itself uncertain; in this article we will assume a factor of two uncertainty, i.e., a range of 0.5 to 2.0×10^{-9} for the mean abundance. In addition, clump-to-clump variations in $X_{\rm HCO^+}$ are expected; we will assume a dispersion of a factor of two. There may be a number of effects that lead to a systematic variation of $X_{\rm HCO^+}$ with environmental conditions. For example, we have recently found (Barnes et al. 2013) that the HCO^+ abundance may be enhanced in the vicinity of ionizing radiation from massive stars, with a possibly lower $X_{\rm HCO^+}$ in the majority of darker, more quiescent clumps. If confirmed, this particular effect would tend to have the effect of increasing the masses quoted here for the more quiescent clumps but would decrease the masses for the minority of vigorously star-forming clumps. Future work to improve the calibration of HCO^+-derived masses is needed. (3) The distance to the sources (the clumps' median distance uncertainty is estimated in Paper I to be 20% based mostly on classical distance estimates to GMC complexes and assuming an association of clumps with a particular GMC complex. Here we use a slightly larger, more conservative value of 30% for the absolute distance uncertainty (see also Paper I for a more extensive discussion of distance estimates), i.e., leading to $\sim$60% uncertainties in M). Combining these uncertainties, we conclude that the absolute mass estimate of any particular clump may be uncertain by as much as a factor of $\sim$3.

To measure the continuum fluxes at various wavelengths coming from the CHaMP HCO^+ clumps, we define the clump size as two times larger than the FWHM ellipse derived in Paper I, i.e., its radial extent is equal to one FWHM at a given position angle. For a two-dimensional Gaussian flux distribution as assumed in Paper I, the area inside this ellipse encloses 93.75% of the total flux. Thus with this definition of clump size we expect to enclose close to 100% of the total HCO^+ flux measured in Paper I and presumably close to 100% of the continuum flux associated with each clump.

The clumps are highly clustered in space so that on a scale of two times the FWHM ellipse the majority of them, ∼70% of the sample, suffer from overlap with a neighboring clump (∼30% overlap on the scale of one times the FWHM ellipse). While the original clump definition from Paper I also used their velocity space information, sometimes nearby clumps also overlap in velocity to some extent. We have developed an approximate method to estimate the fluxes of these clumps where there are image pixels belonging to more than one ellipse. We first calculate the angular distance, normalized by the size of the ellipse, from the overlapped pixel to the center of each clump. This normalized angular distance is defined as $r_{\rm norm} = ((d_x/a)^2 + (d_y/b)^2)^{1/2}$, where d_x and d_y are the angular distance from the overlapped pixel to the minor and major axis of each ellipse, and a and b are the angular sizes of the major and minor axis of the ellipse. The flux of each overlapped pixel is then assigned to its nearest ellipse according to this normalized angular distance.

3.2. Clump and Background Flux Measurements

The *MSX* and *IRAS* data exist for all 303 CHaMP clumps, and these form the basis for our SED measurements. We describe here the method we use to derive the fluxes from the clumps based on these imaging data. We then describe how we utilize the midinfrared IRAC data and the mm data where it is available.

Using the coordinates, sizes, and geometries of the HCO^+ sources, fluxes were deduced first by directly integrating over the images; this total flux is expressed as $F_{\nu,\rm tot}$. However, we expect that some fraction of this flux can come from foreground and background sources along the line of sight that are not associated with the clump. For simplicity we refer to this foreground and background emission as the "background flux," $F_{\nu,b}$. We evaluate $F_{\nu,b}$ as the median pixel value in the region between the clump ellipse (as defined here) and an ellipse that is twice as large (i.e., four times the FWHM size of Paper I), excluding areas that are part of other clumps.

In the end, we derived two fluxes: without and with background subtracted, which are $F_{\nu,\rm tot}$ and $F_\nu = F_{\nu,\rm tot} - F_{\nu,b}$, respectively. The error of the fluxes are estimated from the combination of two terms. The first is the uncertainty in the absolute flux from the particular telescope. The data used here are generally assumed to be accurate to about 20%. The second term is from the background subtraction. Because it is often difficult to estimate the background emission in the Galactic plane, we treat the background level as an error term in our flux error estimation. So the fractional error is $(0.2^2 + (F_{\nu,\rm b}/F_{\nu,\rm tot})^2)^{1/2}$. In the following, we have carried out the analysis for both flux estimates, $F_{\nu,\rm tot}$ and F_ν.

Next we use a two-temperature gray-body model to fit the SED in order to estimate the bolometric fluxes, $F_{\rm tot}$ (no background subtracted) and F (background subtracted; calculated by integrating over the fitted SED and assuming negligible flux escapes in the near-IR and shorter wavelengths), and the temperatures of the clumps, following the method of Hunter et al. (2000) and Faúndez et al. (2004). Each temperature component of the gray-body model is described by

$$F_\nu = \Omega B_\nu(T)\{1 - \exp(-\tau_\nu)\}, \quad (1)$$

where $B_\nu(T) = (2h\nu^3/c^2)/[\exp(h\nu/kT) - 1]$ is the Planck function for the black-body flux density (where c is the speed of light, h is the Planck constant, and k is the Boltzmann constant), Ω is the angular size of the source, and T is the temperature. The dependence of the optical depth, τ_ν, with frequency, ν, is given by

$$\tau_\nu = \left(\frac{\nu}{\nu_0}\right)^\beta, \quad (2)$$

where β is the emissivity index and ν_0 is the turnover frequency.

In this fitting procedure, we explored parameter values in the ranges of T_c = 10–50 K and β_c = 1.0–2.5 for the colder component (subscript "c"). These values of β_c are those expected from laboratory experiments and observational results (see Schnee et al. 2010 and references therein). Also, Faúndez et al. (2004) found β_c to be in this range for their sample of sources. We find ν_0 to generally be in the range 3–30 THz. For the warmer component (subscript "w"), T_w was allowed to have values in the range of 100–300 K, while β_w was fixed to 1 following Hunter et al. (2000) and Faúndez et al. (2004). The choice of $\beta_w = 1$ is motivated both by theoretical calculations and by observational evidence (Whittet 1992, pp. 201–203). The angular size of the colder component, Ω_c was set equal to the angular size of the clump, including accounting for reduction due to overlap with other clumps. For the warmer component the angular size, Ω_w, is derived from the best-fitting result, as it is always smaller than the angular size of the clump.

The values of T_c are not particularly well-constrained by the *IRAS* data, which extend to the longest wavelength of only 100 μm. For those 15 sources where we do have mm fluxes reported from SEST-SIMBA, we examine how the two-temperature gray-body model fit changes when we do make use of the mm flux. Note, for the mm fluxes, not having access to estimates of $F_{\nu,b}$, we assume that background subtraction makes a negligible difference, i.e., $F_{\nu,b} \ll F_\nu$. In Figure 1 we present the SED and model fits of BYF 73 (G286.2+0.2), which is one of the more massive and actively star-forming clumps in the sample (Barnes et al. 2010), as one example to show the effect of the mm flux measurement. The results from only the *MSX* and *IRAS* data are T_c = 35.2, 33.2 K, β_c = 1.45, 1.52, and ν_0 = 101, 31.1 THz, without and with background subtraction, respectively. Adding in the mm flux we now derive T_c = 32.8, 30.4 K, β_c = 1.82, 1.78, and ν_0 = 15.4, 11.1 THz for these same cases. The bolometric flux, obtained by integrating over the model spectrum, changes from (1.32, 1.22) × 10^{-7} erg^{-1} s^{-1} cm^{-2}, without and with background subtraction, respectively, to (1.30, 1.20) × 10^{-7} erg^{-1} s^{-1} cm^{-2} when the mm flux is utilized.

The fitting results for all 15 sources with mm flux measurements using the nonbackground subtraction method are summarized in Table 1. These results show that T_c typically changes by $\lesssim$5 K after including the mm flux.[3] The mean value changes by about 10%. We find that β_c changes from 2.0 ± 0.33 to 1.85 ± 0.41 after utilizing the mm flux. Most importantly, we find that the bolometric fluxes, $F_{\rm tot}$ and F, typically change by $\lesssim$ 10% after including the mm flux. Thus we conclude that the lack of longer wavelength data for the main sample introduces only a modest uncertainty of ∼10% in $F_{\rm tot}$ and F. Note, however, that the limited FIR/submillimeter coverage of the SEDs, even with the SEST-SIMBA data, prevent accurate measurement of T_c, ν_0, and β. This situation will be improved with forthcoming data from the *Herschel* Hi-GAL survey (Molinari et al. 2010).

In this article, we choose not to use the IRAC data for our fiducial SED fitting (although we do examine certain

[3] We note that all 15 of these sources contain, or lie near, luminous young clusters. Therefore it is possible that the remainder of the clumps, many of which are relatively quiescent in their star-forming activity, may have systematically lower T_c (when good longer-wavelength data are included) than this subsample would suggest.

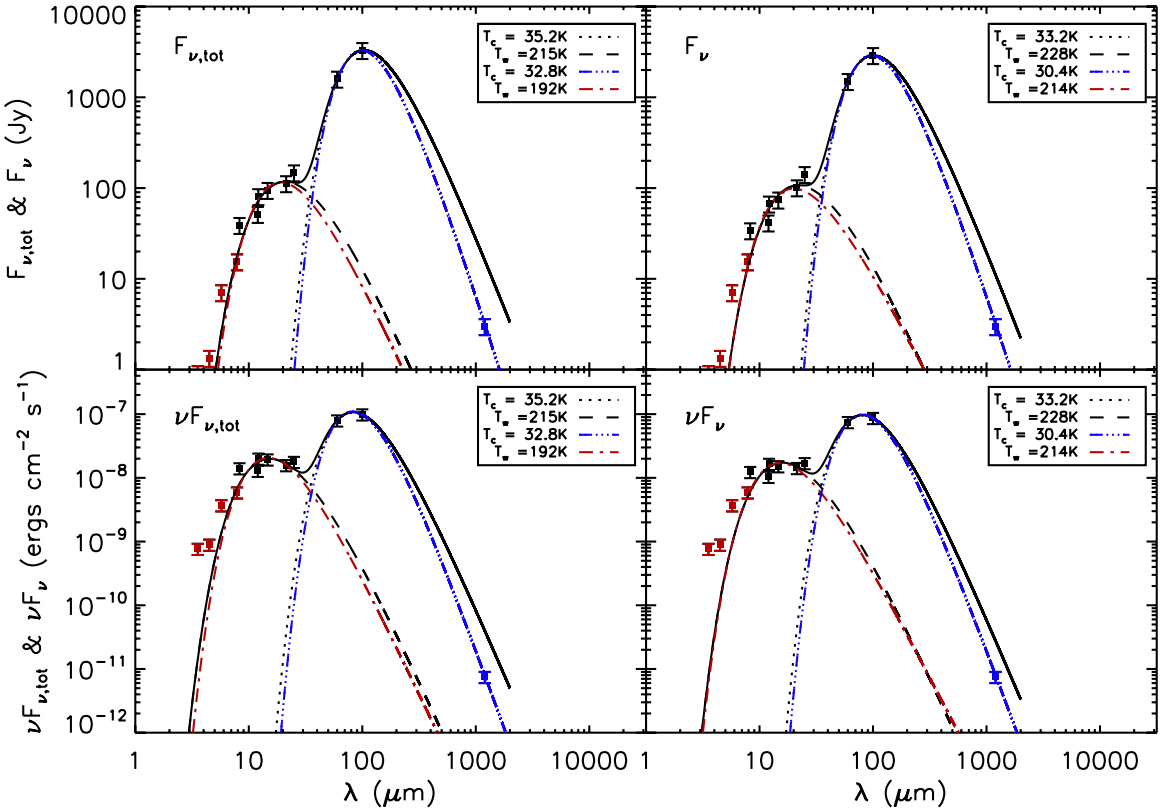

Figure 1. SED fitting results of BYF 73 (G286.2+0.2). (a) Top left: $F_{\nu,\mathrm{tot}}$ (no background subtracted); (b) top right: F_ν (background subtracted); (c) bottom left: $\nu F_{\nu,\mathrm{tot}}$ (no background subtracted); (d) bottom right: νF_ν (background subtracted). The data in order of increasing wavelength are *Spitzer*-IRAC, *MSX*, *IRAS*, SIMBA. In the fiducial case, which is used for the main analysis of the 303 CHaMP clumps, we only use *MSX* and *IRAS* data to find colder component temperatures $T_c = 35.2, 33.2$ K (without and with background subtraction; dotted lines), and $T_w = 215, 228$ K (dashed lines). The totals are shown by the solid lines. Fitting *MSX*, *IRAS*, and the mm SIMBA flux leads to revised model fits with $T_c = 32.8, 30.4$ K (dash-dot-dot-dotted lines). Fitting IRAC, *MSX* and *IRAS* leads to revised model fits with $T_w = 192, 214$ K (dash-dotted lines). In both cases the bolometric fluxes change by $\lesssim$5% from the fiducial case.

(A color version of this figure is available in the online journal.)

Table 1
Effect of 1.2 mm Data on SED Fitting

BYF No.	T_c[a] (K)	log(F)[a] (erg s^{-1} cm^{-2})	T_c[b] (K)	log(F)[b] (erg s^{-1} cm^{-2})
73	35.2	−6.88	32.8	−6.89
126a	37.9	−5.64	37.9	−5.64
126b	35.2	−6.33	37.2	−6.33
126c	30.4	−6.39	31.8	−6.45
128a	36.4	−7.10	34.5	−7.04
128b	39.0	−5.80	39.9	−5.79
131b	37.0	−7.07	39.5	−7.06
131c	50.0	−6.46	41.4	−6.50
131d	39.6	−6.13	41.2	−6.13
131e	49.2	−6.32	42.7	−6.33
132d	37.0	−5.92	39.8	−5.89
132e	31.0	−6.68	37.5	−6.61
162	31.1	−8.46	33.5	−8.52
163a	40.1	−7.12	39.4	−7.12
163b	35.5	−7.48	39.2	−7.49

Notes.
[a] Using *MSX* and *IRAS* data.
[b] Using *MSX*, *IRAS*, and mm data.

correlations of clump properties with the flux in the IRAC bands). The IRAC data are not available for about 10% of the CHaMP clumps (generally those furthest from the midplane), and we wish to maintain the same procedure for all the clumps in the sample. Furthermore, the bolometric luminosity is dominated by the colder component, even for clumps with the most active star formation (see, e.g., Figure 1). For BYF 73, when we compare SED fitting (no background subtraction) with just *MSX*+*IRAS* to that with IRAC+*MSX*+*IRAS* we see that T_c changes from 35.1 K to 35.0 K, T_w changes from 215 K to 230 K, and F changes from 1.323×10^{-7} erg^{-1} s^{-1} cm^{-2} to 1.328×10^{-7} erg^{-1} s^{-1} cm^{-2}.

4. RESULTS

4.1. HCO^+ Masses

In this article we set the clump mass, M, equal to that derived from the analysis of HCO^+(1–0) emission, M_{col} (listed in Column 9 of Table 5, Paper I). The distribution of these masses is presented in Figure 2(a). The masses range from ∼10–10^4 $M_\odot$, with a mean of 723 $M_\odot$ and a median of 427 $M_\odot$. The clump masses and other clump properties are also listed in Table 2. Additional, secondary clump properties are listed in Table 3.

As discussed above, uncertainties in absolute clump mass are likely to be at the level of about a factor of four, mainly due to uncertainties in HCO^+ abundance. We expect relative clump masses are somewhat better determined, especially since a large fraction of the CHaMP clumps are in the Carina spiral arm, with about half in the same η Carinae giant molecular association at a common distance of ∼2.5 kpc.

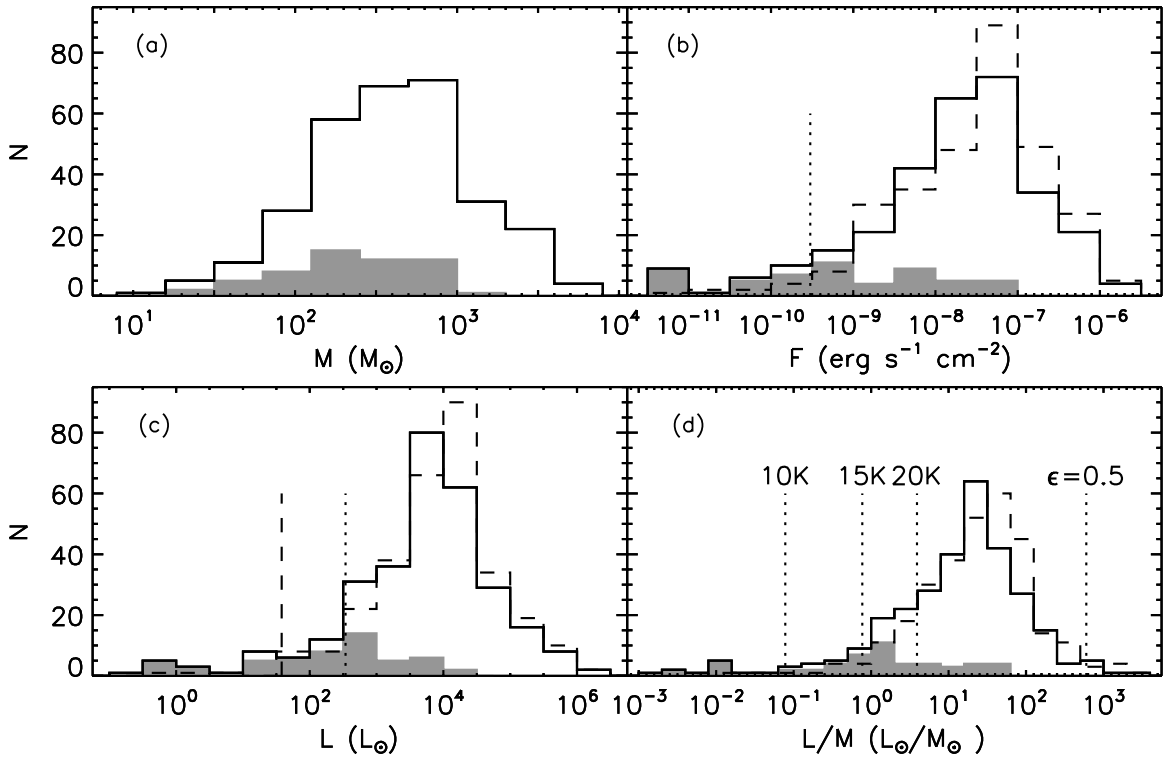

Figure 2. (a) Distribution of the masses (M, estimated from HCO^+(1–0)) of the 303 CHaMP clumps. The gray shaded histogram shows the sources for which the bolometric flux, F, measurements are uncertain due to background subtraction (see (b)). (b) Distribution of the bolometric fluxes (F, solid line, estimated from the two-temperature gray-body fit to the background subtracted SED; $F_{\rm tot}$, dashed line, estimated from the two-temperature gray-body fit to the total SED (no background subtracted)). The gray shaded histogram shows the sources for which the bolometric flux, F, measurements are uncertain due to having *IRAS* 100 μm background fluxes >0.75 of the clump flux. The vertical dotted line shows a bolometric flux of 3×10^{-10} erg^{-1} s^{-1} cm^{-2}, which is our estimate for the 10σ sensitivity flux limit of the *IRAS* data for a clump with typical angular size of 60″. (c) Distribution of bolometric luminosities (L, solid line, estimated from F; $L_{\rm tot}$, dashed line, estimated from $F_{\rm tot}$). The gray shaded histogram, a subset of L, shows the same sources as described in (b) with uncertain flux measurements due to background subtraction. The vertical dashed and dotted lines show the luminosity corresponding to the flux limit shown in (b) for clumps at 2.0 and 6.0 kpc, respectively. (d) Distribution of luminosity to mass ratios (L/M, solid line; $L_{\rm tot}/M$, dashed line). The gray shaded histogram, a subset of L/M, shows the same sources as described in (b) with uncertain flux measurements due to background subtraction. Three vertical dotted lines on the left side show $L/M = 0.078, 0.77, 3.9\ L_\odot/M_\odot$ (from left to right), which corresponds to a gray-body with $T = 10, 15, 20$ K. The vertical dotted line on the right side shows $L/M = 600\ L_\odot/M_\odot$, which corresponds to a clump with an equal mass of gas and stars (i.e., a star formation efficiency $\epsilon \equiv M_*/(M_* + M) = 0.5$) that are on the ZAMS.

4.2. Bolometric Fluxes

The bolometric flux distributions without ($F_{\rm tot}$) and with (F) background subtraction are presented in Figure 2(b). The mean 10σ sensitivity of the four *IRAS* bands are 0.7, 0.65, 0.85, and 3.0 Jy, which correspond to a bolometric flux of about 3×10^{-10} erg^{-1} s^{-1} cm^{-2} for a source with a typical angular size of 60″. This limit is also shown in Figure 2(b). We see that $F_{\rm tot}$ can be detected at better than 10σ for nearly all of the CHaMP clumps. We assume the uncertainty in $F_{\rm tot}$ is about 20% from the absolute flux calibration of the IR observations and about 10% from the two-temperature gray-body model fitting, i.e., adding in quadrature to about 22%.

For the faintest clumps, the total flux from the direction of the clump, $F_{\rm tot}$, can be similar to that of the background (i.e., the region surrounding the clump). The background subtracted flux, F_ν, can thus be very small (or even formally negative) at a particular wavelength. The uncertainty assigned to F_ν is of an order the same level as the background. For deriving bolometric fluxes, the flux at 100 μm is typically most important. Thus we flag those clumps that have a 100 μm background flux that is >0.75 times the clump flux and consider these values of F, L, and L/M to be highly uncertain, i.e., $\gtrsim$100% uncertainties.

4.3. Bolometric Luminosities

Given the clump distances from Paper I and our derived bolometric fluxes, we calculate the bolometric luminosities $L_{\rm tot}$ and L (without and with background subtraction, respectively). The distributions of $L_{\rm tot}$ and L are shown in Figure 2(c).

Adopting a typical distance uncertainty of 30% as explained in Section 3.1, we then estimate an uncertainty in $L_{\rm tot}$ of about 64%. L has somewhat greater uncertainty due to background flux estimation, and again we flag those sources where we expect this source of error dominates.

The mean luminosities are $\langle L_{\rm tot}\rangle = 5.2 \times 10^4\ L_\odot$ and $\langle L\rangle = 4.2 \times 10^4\ L_\odot$. For reference, this is about the luminosity of a 20 $M_\odot$ zero age main sequence (ZAMS) star (Schaller et al. 1992). The median values of $L_{\rm tot}$ and L are $1.06 \times 10^4\ L_\odot$ and $6.2 \times 10^3 L_\odot$, respectively: half of the sample are lower in luminosity than a single 12 $M_\odot$ ZAMS star.

Note that the previous surveys of dust emission toward massive star-forming regions by Mueller et al. (2002) and Faúndez et al. (2004) found $\langle L_{\rm tot}\rangle = 2.5 \times 10^5\ L_\odot$ and $2.3 \times 10^5\ L_\odot$, respectively. These values are much larger that those of the CHaMP clumps. We attribute this difference as being due to the different selection criteria of the samples: CHaMP is a complete sample of dense gas independent of star

Table 2
Primary Physical Properties of the HCO^+(1–0) Clumps[a]

BYF No.	$\log(M)$[b] ($M_\odot$)	$T_{c,tot}$ (K)	$\log(F_{tot})$ (erg s^{-1} cm^{-2})	$\log(L_{tot})$ ($L_\odot$)	$\log(L_{tot}/M)$ ($L_\odot/M_\odot$)	T_c (K)	$\log(F)$ (erg s^{-1} cm^{-2})	$\log(L)$ ($L_\odot$)	$\log(L/M)$ ($L_\odot/M_\odot$)
5a	3.01	33.4	−7.06	4.47	1.46	34.5	−7.07	4.46	1.45
5b	2.13	30.5	−8.10	3.43	1.29	29.5	−8.38	3.15	1.01
5c	2.62	27.8	−7.92	3.61	0.99	30.5	−8.03	3.50	0.87
5d	2.95	34.9	−6.88	4.65	1.70	36.3	−6.89	4.64	1.69
7a	3.12	34.8	−6.62	4.90	1.78	35.8	−6.64	4.91	1.79
7b	2.71	34.7	−6.93	4.60	1.89	35.6	−6.95	4.58	1.87
9	2.65	21.5	−8.50	3.03	0.38	23.0	−8.68	2.85	0.20
11a	2.90	37.8	−7.11	4.42	1.52	34.6	−7.11	4.42	1.52
11b	2.68	32.4	−8.07	3.46	0.77	31.0	−8.19	3.34	0.66
11c	2.10	30.8	−9.88	1.65	−0.45	24.9	−10.08	1.45	−0.65
14*	1.99	24.2	−8.89	2.64	0.65	26.5	−9.28	2.24	0.26
15*	1.78	25.0	−9.38	2.15	0.37	30.5	−9.88	1.65	−0.13
16a	1.46	41.8	−8.12	3.41	1.95	41.1	−8.14	3.39	1.93
16b	2.30	25.8	−8.58	2.95	0.64	22.2	−8.71	2.82	0.51
16c*	2.04	25.2	−8.78	2.75	0.71	29.2	−9.21	2.32	0.28
16d	2.06	32.3	−8.42	3.11	1.04	34.2	−8.50	3.03	0.97
17a	2.11	31.0	−8.19	3.34	1.23	36.0	−8.25	3.28	1.17
17b	2.09	26.7	−8.46	3.07	0.98	29.0	−8.57	2.96	0.87
17c	2.55	25.7	−8.48	3.05	0.50	27.2	−8.67	2.86	0.31
19a*	2.13	27.4	−8.61	2.92	0.78	36.7	−9.03	2.50	0.37
19b	1.94	21.5	−8.70	2.83	0.89	12.8	−8.44	3.09	1.14
20*	2.39	24.5	−8.90	2.63	0.24	29.2	−9.42	2.11	−0.28
22	2.66	27.9	−7.83	3.70	1.04	32.2	−7.91	3.62	0.96
23a	2.65	30.4	−7.65	3.88	1.24	29.0	−7.70	3.83	1.19
23b	2.52	30.9	−7.39	4.14	1.62	30.5	−7.41	4.12	1.60
24	2.57	29.3	−7.53	4.00	1.43	30.8	−7.60	3.92	1.35
25a	3.06	29.7	−7.14	4.39	1.33	34.0	−7.19	4.34	1.28
25b	1.95	30.2	−8.24	3.29	1.34	34.0	−8.38	3.15	1.20
26	2.49	28.0	−7.77	3.75	1.27	32.5	−7.97	3.56	1.07
27*	2.17	26.7	−8.38	3.15	0.98	30.7	−9.06	2.47	0.30
32a	2.40	28.9	−8.57	2.96	0.56	29.0	−8.92	2.61	0.21
32b	2.12	26.9	−8.66	2.87	0.75	31.9	−9.16	2.37	0.25
36a	2.68	30.0	−7.64	3.89	1.21	31.0	−7.85	3.68	1.00
36b	2.81	33.6	−7.39	4.14	1.33	31.4	−7.46	4.07	1.25
36c	2.66	35.3	−7.03	4.50	1.83	36.6	−7.07	4.46	1.80
36d	2.65	29.9	−7.60	3.93	1.28	30.2	−7.74	3.79	1.14
36e	2.20	29.5	−8.17	3.36	1.17	24.1	−8.60	2.93	0.73
37a*	2.14	28.3	−8.52	3.01	0.86	50.0	−9.77	1.76	−0.38
37b*	1.84	29.3	−8.66	2.87	1.03	41.4	−9.66	1.87	0.03
38	2.10	35.0	−7.82	3.30	1.20	35.3	−7.84	3.28	1.18
40a	3.88	42.7	−6.69	5.47	1.59	41.7	−6.70	5.46	1.58
40b	3.70	34.1	−7.25	4.90	1.20	34.3	−7.32	4.83	1.13
40c	3.02	32.9	−7.82	4.33	1.31	34.9	−8.05	4.11	1.08
40d	3.38	34.5	−7.10	5.06	1.68	33.9	−7.13	5.03	1.65
40e	3.53	33.2	−7.36	4.80	1.27	30.7	−7.52	4.64	1.11
40f	3.59	31.9	−7.37	4.78	1.19	30.4	−7.56	4.60	1.01
40g	3.36	32.6	−7.41	4.75	1.39	30.3	−7.57	4.59	1.23
41	3.36	28.0	−7.43	4.73	1.37	30.7	−7.71	4.45	1.09
42a	2.74	28.7	−8.09	4.07	1.33	29.3	−8.35	3.81	1.07
42b	2.78	30.0	−8.35	3.80	1.02	30.8	−8.64	3.52	0.74
47*	2.83	26.6	−8.59	3.37	0.54	28.8	−9.01	2.95	0.12
54a	3.50	41.2	−6.48	5.49	1.99	47.0	−6.49	5.48	1.98
54b	3.78	39.5	−6.53	5.44	1.66	40.7	−6.53	5.43	1.65
54c	3.51	32.9	−6.88	5.09	1.58	28.5	−6.90	5.07	1.56
54d	3.54	42.6	−6.40	5.56	2.02	43.7	−6.41	5.56	2.02
54e	3.37	32.5	−6.81	5.15	1.78	37.6	−6.85	5.12	1.75
54f	3.25	32.7	−7.63	4.34	1.09	36.1	−7.75	4.21	0.97
54g	3.15	25.2	−8.14	3.83	0.68	27.0	−8.41	3.56	0.41
54h	3.17	32.1	−7.83	4.14	0.97	34.3	−8.11	3.86	0.69
56a	3.35	35.6	−7.32	4.65	1.30	37.2	−7.37	4.60	1.25
56b	3.02	26.3	−8.42	3.55	0.53	24.4	−8.54	3.42	0.40
56c*	2.84	22.8	−8.72	3.25	0.40	21.5	−9.14	2.82	−0.02
56d	2.97	29.2	−8.31	3.66	0.69	28.7	−8.49	3.48	0.51
57a	3.05	27.5	−7.86	4.10	1.06	31.0	−7.90	4.06	1.02

Table 2
(Continued.)

BYF No.	$\log(M)^{b}$ ($M_\odot$)	$T_{c,tot}$ (K)	$\log(F_{tot})$ (erg s^{-1} cm^{-2})	$\log(L_{tot})$ ($L_\odot$)	$\log(L_{tot}/M)$ ($L_\odot/M_\odot$)	T_c (K)	$\log(F)$ (erg s^{-1} cm^{-2})	$\log(L)$ ($L_\odot$)	$\log(L/M)$ ($L_\odot/M_\odot$)
57b	2.54	21.2	−8.69	3.27	0.73	16.9	−8.77	3.20	0.65
60a	2.51	22.5	−8.54	3.43	0.92	24.4	−8.92	3.05	0.54
60b*	2.25	21.6	−8.95	3.02	0.77	26.4	−9.57	2.39	0.14
61a*	2.48	26.2	−8.34	2.98	0.49	27.3	−8.70	2.61	0.13
61b*	2.40	27.8	−8.30	3.02	0.62	25.5	−8.65	2.66	0.26
62	2.36	14.5	−8.87	2.44	0.08	12.8	−8.44	2.88	0.52
63*	2.24	26.1	−8.73	2.59	0.34	28.0	−9.25	2.07	−0.18
66	2.49	25.4	−7.40	3.91	1.42	23.5	−8.88	2.43	−0.06
67	2.63	24.0	−8.15	3.17	0.53	22.8	−8.52	2.79	0.16
68	3.43	24.4	−6.97	4.35	0.92	29.6	−7.10	4.22	0.79
69	2.55	30.3	−7.18	4.13	1.58	30.3	−7.34	3.98	1.43
70a	2.94	34.7	−6.93	4.39	1.44	35.8	−7.04	4.28	1.33
70b	3.05	35.3	−6.99	4.32	1.27	37.6	−7.11	4.21	1.16
71	2.63	30.5	−7.43	3.88	1.25	31.1	−7.82	3.49	0.86
72	3.38	27.5	−7.10	4.22	0.84	31.7	−7.32	3.99	0.61
73	3.16	31.3	−6.87	4.44	1.28	34.8	−6.90	4.41	1.25
76	2.76	24.5	−7.53	3.78	1.03	21.4	−7.43	3.89	1.13
77a	2.93	28.1	−7.26	4.05	1.12	29.5	−7.79	3.52	0.59
77b	3.27	33.2	−7.25	4.07	0.80	31.5	−7.32	3.99	0.72
77c	3.24	33.1	−6.71	4.60	1.36	36.0	−6.79	4.53	1.29
77d	2.68	34.5	−7.13	4.18	1.50	33.5	−7.28	4.03	1.35
78a	2.68	26.7	−7.29	4.03	1.35	28.0	−8.08	3.24	0.56
78b	3.01	26.7	−7.42	3.90	0.89	28.5	−7.76	3.55	0.55
78c*	2.62	23.2	−8.30	3.02	0.40	23.8	−8.77	2.55	−0.07
79a	2.82	31.4	−7.85	3.47	0.65	29.6	−8.06	3.26	0.44
79b	2.63	31.3	−7.56	3.75	1.12	31.3	−7.83	3.49	0.85
79c	2.74	29.6	−8.07	3.25	0.51	29.3	−8.36	2.95	0.21
83	2.74	32.6	−7.14	4.18	1.44	32.0	−7.37	3.94	1.20
85a	2.96	26.6	−7.70	3.61	0.65	19.6	−7.60	3.72	0.75
85b	3.01	30.1	−7.48	3.84	0.83	28.5	−7.90	3.42	0.41
85c	2.30	29.6	−8.11	3.21	0.91	25.1	−8.57	2.75	0.45
86a	2.78	30.5	−7.57	3.75	0.97	34.1	−7.92	3.39	0.61
86b	2.57	31.9	−7.48	3.84	1.27	33.3	−7.67	3.65	1.08
87	3.12	29.4	−7.26	4.06	0.94	27.2	−7.65	3.67	0.54
88	2.87	35.2	−6.91	4.41	1.54	37.6	−7.18	4.14	1.27
89a	2.45	30.2	−7.86	3.45	1.01	26.0	−8.11	3.21	0.76
89b	3.07	31.6	−7.05	4.26	1.20	25.3	−7.07	4.24	1.18
89c	2.14	30.4	−8.02	3.30	1.15	27.0	−8.22	3.10	0.95
90a	2.87	32.7	−6.83	4.48	1.61	32.0	−7.16	4.16	1.29
90b	2.78	33.8	−6.98	4.33	1.55	32.9	−7.28	4.04	1.26
90c	2.53	34.5	−6.76	4.55	2.03	34.6	−6.93	4.38	1.86
91a	3.24	31.2	−6.56	4.75	1.51	35.0	−6.77	4.54	1.30
91b	2.43	31.7	−7.38	3.94	1.50	29.8	−7.73	3.58	1.15
91c*	2.58	28.2	−7.95	3.36	0.79	19.5	−8.33	2.98	0.41
91d*	2.82	27.9	−8.49	2.82	0.01	11.9	−8.50	2.81	−0.01
91e	2.53	33.8	−7.19	4.12	1.60	29.1	−7.55	3.76	1.23
92a*	2.85	28.1	−7.59	3.73	0.87	29.6	−8.09	3.22	0.37
92b*	2.97	30.0	−7.28	4.03	1.06	26.5	−7.88	3.43	0.46
93a	3.13	34.6	−6.47	4.85	1.72	37.8	−6.66	4.66	1.53
93b	2.82	35.5	−6.49	4.82	2.00	38.5	−6.66	4.66	1.84
93c	2.56	34.3	−7.05	4.27	1.71	31.8	−7.35	3.96	1.40
94a	2.98	34.3	−6.83	4.48	1.50	33.2	−7.07	4.25	1.26
94b	2.85	31.6	−7.02	4.30	1.45	29.3	−7.41	3.90	1.05
94c	2.79	33.6	−7.06	4.25	1.46	32.9	−7.28	4.04	1.25
94d	2.84	33.8	−6.65	4.66	1.82	34.4	−6.93	4.38	1.54
94e	2.19	35.1	−7.30	4.02	1.83	33.5	−7.61	3.70	1.51
94f	2.01	34.8	−7.43	3.88	1.87	33.4	−7.62	3.69	1.68
94g	2.40	34.6	−6.87	4.44	2.04	34.9	−7.00	4.31	1.92
94h	2.56	35.4	−6.32	5.00	2.44	41.6	−6.40	4.92	2.36
95a	2.94	35.2	−7.21	4.10	1.16	32.7	−7.54	3.77	0.83
95b	2.17	35.2	−6.74	4.57	2.40	35.3	−7.01	4.30	2.13
95c*	2.28	34.1	−7.61	3.70	1.42	14.4	−7.83	3.48	1.20
96	2.81	30.0	−7.55	3.76	0.95	19.7	−7.57	3.74	0.94
97	2.77	33.0	−6.80	4.52	1.75	34.1	−7.04	4.27	1.50

Table 2
(Continued.)

BYF No.	$\log(M)^{b}$ ($M_\odot$)	$T_{c,tot}$ (K)	$\log(F_{tot})$ (erg s^{-1} cm^{-2})	$\log(L_{tot})$ ($L_\odot$)	$\log(L_{tot}/M)$ ($L_\odot/M_\odot$)	T_c (K)	$\log(F)$ (erg s^{-1} cm^{-2})	$\log(L)$ ($L_\odot$)	$\log(L/M)$ ($L_\odot/M_\odot$)
98a	2.93	39.6	−6.11	5.20	2.28	44.7	−6.31	5.00	2.08
98b*	2.53	39.6	−7.39	3.93	1.39	46.1	−8.04	3.27	0.74
98c*	1.89	45.1	−10.95	0.37	−1.53	10.0	−10.95	0.37	−1.52
99a	2.83	35.5	−6.87	4.44	1.61	35.7	−6.94	4.37	1.55
99b	2.75	35.5	−6.76	4.56	1.80	39.3	−6.83	4.48	1.73
99c	2.33	41.8	−6.86	4.46	2.13	41.7	−6.92	4.39	2.06
99d	1.88	38.2	−6.90	4.41	2.54	32.2	−7.29	4.03	2.15
99e	2.41	38.1	−7.40	3.91	1.50	37.5	−7.51	3.80	1.39
99f	1.99	42.9	−6.94	4.38	2.38	50.0	−7.07	4.24	2.25
99g	2.46	46.6	−6.21	5.11	2.65	50.0	−6.32	5.00	2.54
99h*	2.31	43.1	−7.15	4.16	1.85	47.4	−7.24	4.07	1.76
99i	2.10	43.5	−6.33	4.98	2.88	45.2	−6.44	4.88	2.78
99j	3.18	41.0	−6.21	5.11	1.93	42.9	−6.27	5.04	1.86
99k	2.91	40.1	−6.02	5.30	2.38	47.0	−6.16	5.16	2.25
99l	3.44	36.4	−6.32	5.00	1.56	40.2	−6.48	4.83	1.39
99m	3.52	39.4	−5.79	5.53	2.00	50.0	−5.83	5.48	1.96
99n	2.71	36.4	−6.57	4.74	2.03	37.5	−6.72	4.59	1.88
99o	2.46	33.4	−7.17	4.15	1.69	32.0	−7.44	3.88	1.42
99p	2.11	38.3	−7.05	4.26	2.16	41.9	−7.29	4.02	1.91
99q	2.51	36.8	−7.30	4.02	1.51	38.8	−7.52	3.79	1.29
99r	2.61	33.4	−6.46	4.85	2.24	37.7	−6.72	4.60	1.99
100a	3.04	34.2	−6.56	4.76	1.72	34.8	−6.90	4.41	1.37
100b	2.83	37.6	−6.20	5.11	2.28	40.8	−6.37	4.95	2.11
100c	1.96	39.7	−7.03	4.29	2.33	37.1	−7.09	4.22	2.27
100d*	2.53	34.8	−7.09	4.22	1.70	32.2	−7.60	3.71	1.18
100e*	2.43	36.0	−7.05	4.27	1.83	38.7	−7.60	3.72	1.28
100f	1.97	31.8	−8.09	3.22	1.25	28.9	−8.62	2.70	0.72
100g*	2.25	32.0	−8.15	3.16	0.92	12.8	−8.45	2.86	0.62
101a	2.17	35.6	−7.42	3.89	1.72	34.0	−7.59	3.73	1.55
101b	2.32	36.4	−7.18	4.14	1.82	35.5	−7.36	3.96	1.64
102a	2.24	38.7	−7.50	3.82	1.58	38.1	−7.79	3.53	1.29
102b	2.43	38.6	−6.85	4.47	2.03	36.2	−7.10	4.22	1.78
102c*	1.75	37.4	−7.80	3.52	1.77	41.5	−8.28	3.04	1.29
102d	1.56	40.0	−7.50	3.81	2.26	41.1	−7.97	3.35	1.79
103a*	2.41	38.8	−6.94	4.37	1.96	48.2	−7.36	3.96	1.54
103b*	2.43	39.5	−7.01	4.30	1.88	42.5	−7.35	3.97	1.54
103c	2.39	38.2	−6.36	4.95	2.56	40.5	−6.56	4.75	2.36
103d	2.48	39.0	−7.15	4.17	1.69	37.7	−7.27	4.04	1.56
103e	1.77	38.4	−7.12	4.20	2.43	35.8	−7.29	4.03	2.26
104a	1.40	42.1	−7.05	4.27	2.87	32.8	−7.42	3.89	2.50
104b	2.50	44.9	−6.26	5.05	2.55	47.6	−6.46	4.86	2.36
104c	2.43	43.5	−6.19	5.12	2.69	46.7	−6.30	5.02	2.59
105a	2.37	34.6	−7.51	3.80	1.43	21.1	−7.48	3.83	1.47
105b	3.16	35.9	−6.13	5.18	2.02	40.3	−6.39	4.92	1.76
105c*	2.64	29.2	−8.45	2.86	0.22	35.6	−11.42	−0.10	−2.74
105d*	2.92	35.2	−6.97	4.34	1.43	26.0	−7.48	3.84	0.92
105e	2.27	35.2	−7.17	4.15	1.88	31.8	−7.43	3.88	1.61
106a	2.47	36.0	−7.19	4.13	1.66	34.2	−7.40	3.91	1.44
106b	2.22	38.3	−7.19	4.12	1.90	37.0	−7.35	3.96	1.74
106c*	1.72	37.7	−8.56	2.76	1.04	35.6	−11.42	−0.10	−1.82
107a	2.22	37.4	−7.14	4.18	1.96	36.2	−7.25	4.07	1.85
107b	2.72	36.2	−6.71	4.60	1.88	36.9	−6.86	4.45	1.73
107c	2.54	34.8	−6.52	4.80	2.26	36.5	−6.68	4.64	2.10
107d	2.17	34.7	−7.05	4.26	2.10	32.5	−7.19	4.12	1.96
107e	2.73	36.9	−6.93	4.39	1.66	36.3	−7.26	4.05	1.32
107f	2.63	35.8	−6.95	4.37	1.74	32.7	−7.14	4.18	1.55
107g	2.52	36.4	−6.98	4.33	1.81	31.7	−7.29	4.02	1.50
107h*	2.35	33.3	−7.18	4.14	1.79	23.2	−7.30	4.01	1.66
107i*	1.88	36.3	−7.80	3.51	1.64	25.8	−8.38	2.93	1.06
108a	2.49	34.7	−7.69	3.62	1.14	29.7	−8.17	3.15	0.66
108b	2.93	34.0	−6.57	4.75	1.82	36.3	−6.77	4.54	1.62
108c*	2.24	35.1	−7.96	3.36	1.12	35.3	−8.41	2.91	0.67
108d*	1.96	33.8	−7.47	3.85	1.89	26.5	−8.49	2.82	0.86
109a	2.94	42.0	−6.88	4.43	1.49	39.4	−6.94	4.38	1.44

Table 2
(Continued.)

BYF No.	$\log(M)^{b}$ ($M_\odot$)	$T_{c,tot}$ (K)	$\log(F_{tot})$ (erg s^{-1} cm^{-2})	$\log(L_{tot})$ ($L_\odot$)	$\log(L_{tot}/M)$ ($L_\odot/M_\odot$)	T_c (K)	$\log(F)$ (erg s^{-1} cm^{-2})	$\log(L)$ ($L_\odot$)	$\log(L/M)$ ($L_\odot/M_\odot$)
109b	2.35	34.4	−7.45	3.87	1.52	35.6	−7.54	3.77	1.42
109c	2.33	34.7	−7.44	3.88	1.54	30.5	−7.75	3.56	1.23
109d	1.99	33.4	−7.48	3.83	1.84	27.3	−7.66	3.65	1.66
109e	1.40	38.2	−7.40	3.92	2.52	38.9	−7.49	3.83	2.43
109f*	2.32	38.1	−7.60	3.71	1.39	18.1	−7.73	3.58	1.26
110a	2.93	35.1	−6.46	4.86	1.93	39.4	−6.61	4.70	1.77
110b	2.12	36.9	−7.36	3.95	1.84	36.4	−7.59	3.73	1.61
111a	3.53	33.1	−6.23	5.08	1.56	39.0	−6.35	4.97	1.44
111b	2.25	36.3	−7.48	3.84	1.58	35.9	−7.66	3.66	1.40
111c	1.92	33.8	−7.92	3.40	1.47	31.9	−8.21	3.10	1.18
111d	2.72	29.2	−7.00	4.31	1.59	30.5	−7.27	4.04	1.32
112*	2.69	31.0	−7.66	3.66	0.97	26.9	−8.32	2.99	0.30
113a	2.11	38.4	−7.23	4.09	1.98	38.3	−7.40	3.92	1.81
113b	1.96	39.5	−7.01	4.31	2.35	38.7	−7.12	4.20	2.24
114a	2.35	32.9	−7.28	4.04	1.69	31.0	−7.58	3.73	1.38
114b	2.30	37.5	−7.50	3.82	1.52	31.7	−7.70	3.61	1.31
114c	2.08	34.2	−7.27	4.05	1.97	35.0	−7.62	3.69	1.61
115a*	2.34	32.7	−8.89	2.43	0.08	35.6	−11.42	−0.10	−2.45
115b	1.94	35.7	−7.34	3.98	2.04	35.7	−7.48	3.84	1.90
115c	1.57	33.8	−7.72	3.59	2.02	34.0	−7.88	3.44	1.87
116a	2.12	33.6	−7.77	3.54	1.42	32.7	−8.24	3.08	0.95
116b	1.72	33.7	−7.87	3.44	1.73	32.6	−8.31	3.00	1.29
116c	2.10	34.3	−7.52	3.79	1.70	34.7	−7.83	3.48	1.38
117a	2.77	33.0	−6.96	4.35	1.58	30.7	−7.49	3.83	1.05
117b	2.46	34.8	−7.45	3.87	1.41	32.7	−7.79	3.52	1.07
117c*	1.85	30.6	−11.42	−0.10	−1.95	35.6	−11.42	−0.10	−1.95
117d	2.19	33.8	−7.48	3.83	1.64	32.4	−7.70	3.61	1.42
117e	2.45	34.3	−7.19	4.12	1.67	32.7	−7.44	3.88	1.42
118a	2.83	32.3	−7.61	3.71	0.88	35.0	−7.68	3.63	0.80
118b	2.39	33.4	−7.37	3.95	1.56	31.2	−7.61	3.71	1.32
118c	2.70	34.5	−6.99	4.32	1.62	33.5	−7.18	4.13	1.43
123a	2.47	25.2	−9.42	2.77	0.30	23.2	−9.64	2.54	0.08
123b*	2.75	26.1	−9.71	2.47	−0.28	13.1	−9.79	2.39	−0.36
123c*	2.70	23.8	−10.17	2.01	−0.69	35.6	−11.42	0.77	−1.93
123d*	2.42	22.6	−9.84	2.34	−0.08	14.8	−10.44	1.75	−0.67
126a	3.87	37.9	−5.56	5.72	1.85	50.0	−5.56	5.72	1.85
126b	2.82	37.2	−6.37	4.91	2.09	43.1	−6.40	4.88	2.06
126c	3.14	31.8	−6.26	5.02	1.88	40.5	−6.27	5.01	1.87
126d	2.64	39.9	−6.82	4.46	1.81	44.1	−6.88	4.40	1.76
126e	2.96	34.3	−6.75	4.52	1.57	37.6	−6.82	4.46	1.51
127*	1.28	20.7	−8.50	2.10	0.83	35.6	−11.42	−0.82	−2.09
128a	3.37	29.7	−7.03	4.25	0.88	31.7	−7.15	4.13	0.76
128b	3.46	34.5	−5.74	5.54	2.09	50.0	−5.75	5.53	2.08
128c	2.93	30.5	−7.06	4.22	1.29	31.8	−7.11	4.17	1.23
128d	2.83	37.4	−6.75	4.53	1.70	37.7	−6.79	4.49	1.66
128e	2.78	33.6	−7.11	4.17	1.39	33.4	−7.22	4.06	1.28
129a*	1.18	29.6	−8.82	1.85	0.68	24.1	−9.50	1.18	0.00
129b*	1.26	31.5	−8.70	1.97	0.72	30.4	−9.39	1.29	0.03
130a	2.18	24.9	−8.63	2.65	0.47	28.6	−8.76	2.52	0.33
130b	2.21	24.9	−8.68	2.60	0.39	29.8	−8.91	2.37	0.16
131a	3.53	39.5	−6.84	5.24	1.71	37.0	−7.05	5.02	1.49
131b	3.17	39.5	−6.50	5.58	2.41	38.7	−6.73	5.34	2.17
131c	3.32	41.4	−6.27	5.81	2.49	43.3	−6.42	5.66	2.34
131d	3.05	41.2	−5.98	6.10	3.04	41.3	−6.06	6.01	2.96
131e	2.79	42.7	−6.10	5.98	3.19	43.9	−6.14	5.93	3.14
131f	3.38	34.0	−6.77	5.31	1.93	31.2	−6.74	5.34	1.96
131g	3.18	31.1	−7.12	4.95	1.77	31.9	−7.32	4.75	1.57
131h	2.98	34.2	−7.19	4.88	1.90	32.9	−7.44	4.63	1.65
131i	2.45	33.5	−7.90	4.18	1.72	29.8	−8.34	3.73	1.28
132a	3.29	40.5	−6.46	5.61	2.32	41.3	−6.56	5.52	2.22
132b	2.64	35.7	−6.36	5.72	3.08	42.4	−6.44	5.64	3.00
132c	2.27	39.1	−6.68	5.40	3.13	36.9	−6.81	5.26	2.99
132d	3.36	39.8	−5.86	6.22	2.86	40.6	−5.92	6.16	2.80
132e	2.50	37.5	−6.16	5.92	3.42	30.9	−6.21	5.87	3.37

Table 2
(Continued.)

BYF No.	log(M)[b] ($M_\odot$)	$T_{c,tot}$ (K)	log(F_{tot}) (erg s^{-1} cm^{-2})	log(L_{tot}) ($L_\odot$)	log(L_{tot}/M) ($L_\odot/M_\odot$)	T_c (K)	log(F) (erg s^{-1} cm^{-2})	log(L) ($L_\odot$)	log(L/M) ($L_\odot/M_\odot$)
134a*	2.32	25.2	−9.38	1.90	−0.41	20.6	−9.89	1.39	−0.92
134b	2.03	22.7	−9.55	1.73	−0.29	23.4	−9.99	1.29	−0.74
134c	1.96	22.1	−9.43	1.84	−0.11	22.1	−9.79	1.49	−0.47
141a	2.03	29.5	−8.19	3.09	1.07	31.0	−8.36	2.92	0.89
141b	1.63	24.5	−8.21	3.07	1.44	27.6	−8.32	2.96	1.33
142a	2.04	35.8	−7.56	3.72	1.68	35.9	−7.58	3.70	1.66
142b	2.05	31.2	−7.82	3.46	1.41	32.2	−7.90	3.38	1.33
144a*	1.71	27.3	−9.50	1.78	0.07	23.4	−10.11	1.17	−0.54
144b*	2.04	27.7	−9.05	2.23	0.19	25.2	−10.07	1.21	−0.83
144c*	1.72	24.1	−10.65	0.63	−1.08	35.6	−11.42	−0.14	−1.85
149a	2.57	33.8	−6.73	4.55	1.98	38.4	−6.74	4.54	1.96
149b	1.70	31.0	−7.42	3.86	2.16	31.9	−7.50	3.78	2.08
150	2.45	29.9	−7.48	3.80	1.36	31.3	−7.67	3.61	1.17
161	2.37	34.4	−7.39	3.89	1.52	34.2	−7.55	3.73	1.36
162	2.66	33.5	−7.27	4.00	1.34	33.1	−7.42	3.86	1.20
163a	2.78	39.4	−6.92	4.36	1.58	38.0	−6.95	4.33	1.55
163b	2.65	39.2	−7.27	4.01	1.36	36.2	−7.32	3.96	1.31
163c	2.76	35.8	−7.13	4.15	1.39	36.8	−7.30	3.98	1.21
165a	2.53	35.1	−7.44	3.84	1.31	34.6	−7.54	3.74	1.21
165b	2.68	33.3	−6.96	4.31	1.63	34.8	−7.04	4.24	1.55
167a	2.26	30.3	−7.61	3.67	1.41	29.3	−7.70	3.58	1.31
167b	2.64	32.5	−7.08	4.20	1.55	32.8	−7.19	4.09	1.45
167c	2.17	31.1	−7.56	3.72	1.54	30.6	−7.70	3.58	1.41
183	2.78	23.6	−8.95	2.91	0.13	31.2	−9.37	2.49	−0.29
185	2.08	46.3	−7.45	4.41	2.33	41.8	−7.46	4.40	2.33
188*	2.72	23.2	−8.86	3.00	0.28	17.3	−9.25	2.62	−0.11
190a	2.75	27.1	−8.24	3.62	0.87	27.8	−8.31	3.55	0.80
190b	2.74	27.2	−8.02	3.84	1.10	30.1	−8.05	3.81	1.07
199a	2.89	26.3	−8.05	3.81	0.92	29.6	−8.19	3.68	0.79
199b	2.26	24.2	−7.65	4.22	1.95	19.1	−8.19	3.68	1.41
201a	2.71	29.9	−7.95	3.91	1.20	28.7	−8.22	3.65	0.94
201b	2.91	29.8	−7.51	4.35	1.44	29.2	−7.77	4.09	1.18
202a	3.52	24.0	−8.89	2.98	−0.55	24.7	−9.29	2.58	−0.95
202b*	2.79	24.8	−8.84	3.02	0.23	44.4	−10.20	1.66	−1.13
202c	3.02	31.6	−7.60	4.27	1.25	31.6	−7.65	4.22	1.20
202d	2.88	25.7	−8.23	3.63	0.75	25.1	−8.42	3.44	0.56
202e	2.67	25.9	−8.58	3.28	0.62	27.3	−8.76	3.10	0.43
202f*	2.71	25.3	−9.12	2.74	0.03	35.6	−11.42	0.45	−2.26
202g*	2.73	26.1	−8.80	3.07	0.34	24.0	−9.56	2.31	−0.42
202h*	3.00	23.3	−10.32	1.54	−1.46	10.0	−10.32	1.54	−1.46
202i*	2.92	23.0	−9.25	2.61	−0.31	35.6	−11.42	0.45	−2.48
203a	2.92	32.7	−7.89	3.98	1.06	35.9	−7.92	3.94	1.02
203b	2.79	25.1	−8.32	3.55	0.76	24.8	−8.40	3.46	0.67
203c	3.21	31.6	−7.56	4.30	1.09	31.7	−7.58	4.28	1.07
203d	2.90	34.5	−7.65	4.21	1.31	35.3	−7.67	4.20	1.29
208a	3.18	23.8	−8.17	3.69	0.51	20.8	−8.27	3.59	0.41
208b	2.51	23.3	−8.90	2.96	0.45	23.8	−9.09	2.77	0.26

Notes.
[a] Here $T_{c,tot}$ and L_{tot} are the colder component temperatures and infrared luminosities using the nonbackground subtracted method. T_c and L are derived using the background subtracted method.
[b] The mass log(M) is from Paper I.
* Clumps with uncertain measurements of L due to *IRAS* 100 μm background subtraction (see Figure 2(b)).

(This table is also available in a machine-readable form in the online journal.)

formation activity, while these other surveys were selected based on (massive) star formation indicators.

4.4. Luminosity-to-Mass Ratios

During the evolution of star-forming clumps, i.e., the formation of star clusters, the gas mass will decrease due to incorporation into stars and dispersal by feedback, causing the luminosity-to-mass ratio to increase. So L/M should be an evolutionary indicator of the star cluster formation process. The distribution of L/M is shown in Figure 2(d).

Three dotted vertical lines at $L/M = 0.078, 0.77, 3.9\ L_\odot/M_\odot$ are used to show the values expected of clouds with dust temperatures of $T = 10, 15, 20$ K, which can be achieved in starless clumps via external heating, as evidenced by temperature measurements of Infrared Dark Clouds (e.g., Pillai et al. 2006).

Table 3
Secondary Physical Properties of the HCO^+(1–0) Clumps

BYF No.	$\log(F_{\rm w})$ (erg s^{-1} cm^{-2})	$\log(F_{\rm w,tot})$ (erg s^{-1} cm^{-2})	$\log(F_{\rm IRAC})$ (erg s^{-1} cm^{-2})	$\log(F_{\rm IRAC,tot})$ (erg s^{-1} cm^{-2})	$\log(I_{\rm IRAC})$ (erg s^{-1} cm^{-2} sr^{-1})	$\log(I_{\rm IRAC,tot})$ (erg s^{-1} cm^{-2} sr^{-1})	$T_{\rm bol}$ (K)	$T_{\rm bol,tot}$ (K)	Σ (g cm^{-2})	$\sigma_{\rm v}$ (km s^{-1})	$\alpha_{\rm vir}$	$\log(L_{\rm HCO^+(1-0)})$ (K km s^{-1} pc^{-2})
5a	−7.65	−7.68	−8.68	−8.50	−2.78	−2.60	99	93	0.033	1.90	6.1	1.43
5b	−8.94	−8.80	−9.95	−9.47	−3.23	−2.75	106	104	0.029	3.10	54.4	0.37
5c	−8.57	−8.59	−9.44	−9.18	−3.21	−2.95	107	108	0.029	3.00	26.5	0.76
5d	−7.42	−7.48	−7.84	−7.81	−2.06	−2.03	138	136	0.022	2.60	14.7	1.15

Notes. $\sigma_{\rm v}$ and $\alpha^b_{\rm vir}$ are from Paper I.

(This table is available in its entirety in a machine-readable form in the online journal. A portion is shown here for guidance regarding its form and content.)

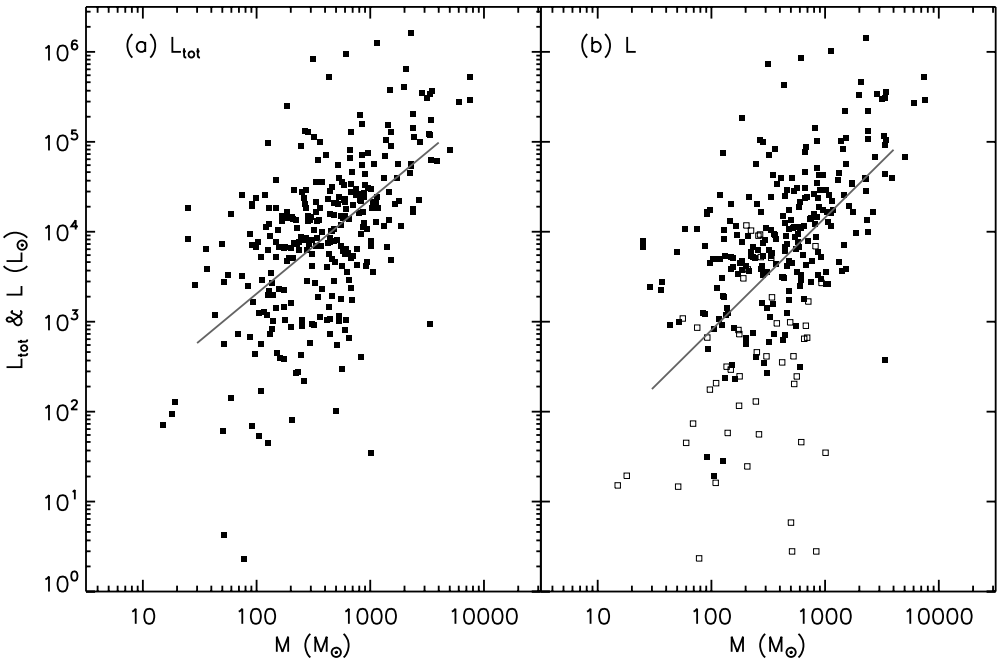

Figure 3. (a) Correlation of L_{tot} with M, with best-fit relation $L_{tot}/L_\odot = 16.2 \times (M/M_\odot)^{1.05}$ shown with a Spearman rank correlation coefficient of 0.54 and a 1.2×10^{-24} probability for a chance correlation. (b) Correlation of L with M, with best-fit relation $L/L_\odot = 3.0 \times (M/M_\odot)^{1.25}$ shown with a Spearman rank correlation coefficient of 0.55 and a 7.2×10^{-25} probability for a chance correlation. Open squares show clumps with uncertain measurements of F due to *IRAS* 100 μm background subtraction (see Figure 2(b)). Note, these are still used to help define the correlation; their larger uncertainties lead to an asymmetric distribution of points about the best-fit relation.

These values are calculated via

$$\frac{L/M}{L_\odot/M_\odot} = \frac{4\pi}{\Sigma}\int B_\nu(1-\exp(-\tau_\nu)\,\mathrm{d}\nu \rightarrow 0.0778\left(\frac{T}{10\,\mathrm{K}}\right)^{5.65}, \quad (3)$$

where the latter evaluation is based on integrating the opacities of the Ossenkopf & Henning (1994) moderately coagulated thin ice mantle dust model (and adopting a gas-to-dust mass ratio of 155) for clouds with $0.01 < \Sigma/\mathrm{g\,cm^{-2}} < 1$ and $10 < T/\mathrm{K} < 20$ (there is a modest dependence of L/M on $\Sigma^{0.02}$, which we ignore, normalizing the numerical factor of Equation (3) to $\Sigma = 0.03\,\mathrm{g\,cm^{-2}}$, typical of the CHaMP clump sample). Values of $L/M \sim 1 L_\odot/M_\odot$ are thus expected to define the lower end of the L/M distribution, as is observed.

To understand the upper end of the observed distribution, consider a clump with an equal mass of gas and stars that are on the ZAMS. For a Salpeter initial mass function (IMF) down to $0.1 M_\odot$, this will have $L/M \sim 600 L_\odot/M_\odot$ (Leitherer et al. 1999; Tan & McKee 2002). Other IMFs typically considered for Galactic star-forming regions give similar numbers to within about a factor of two. This value is close to the upper end of the distribution of L/M shown in Figure 2(d). Note that as the gas mass goes to very small values, L/M should rise far above $600 L_\odot/M_\odot$. However, in this case a smaller fraction of the bolometric luminosity will be reradiated in the MIR and FIR, and so would be missed by our analysis. Also such "revealed" clusters with small amounts of dense gas would not tend to be objects in the CHaMP sample, which is complete only on the basis of emission of dense gas tracers.

To investigate the relation between bolometric luminosity and gas mass (i.e., how luminosity depends on mass), we also show the correlation between L_{tot} and M in Figure 3(a) and the correlation between L and M in Figure 3(b). The best-fit power-law results (e.g., following methodology of Kelly 2007) are as follows:

$$L_{tot}/L_\odot = 16.2(\pm 9.5) \times (M/M_\odot)^{1.05\pm 0.09} \quad (4)$$

with Spearman rank correlation coefficient $r_s = 0.54$ and probability for a chance correlation $p_s \ll 10^{-4}$ (formally $p_s = 1.2 \times 10^{-24}$, but this value depends sensitively on the assumed shape of the tails of the distribution functions, which are not well-defined for real data sets) for the no background subtraction method and

$$L/L_\odot = 3.0(\pm 1.8) \times (M/M_\odot)^{1.25\pm 0.11} \quad (5)$$

with $r_s = 0.55$ and $p_s \ll 10^{-4}$ (formally $p_s = 7.2 \times 10^{-25}$; note that the open symbols in Figure 3(b) have larger uncertainties, explaining the asymmetric distribution of points about the best-fit relation) for the background subtraction method. Both show significant positive correlations. The more massive the clump is, the more luminous it tends to be.

The mean, median, and standard deviation of $\log(L_{tot}/M/[L_\odot/M_\odot])$ are 1.34, 1.43, and 0.77, respectively, for the nonbackground subtraction method. For the background subtraction method, the mean, median, and standard deviation of $\log(L/M/[L_\odot/M_\odot])$ are 1.06, 1.25, and 0.97, respectively.

Molinari et al. (2008) have studied the SEDs of 42 potentially massive individual young stellar objects (YSOs). By fitting the SEDs with YSOs models they obtained the bolometric luminosity and envelope mass, M_{env}. They presented the L_{bol}–M_{env} diagram as a tool to diagnose the pre-MS evolution of massive YSOs. For their sample, the mean, median, and standard deviation of $\log(L/M)$ are 1.91, 1.77, and 0.66, respectively. This illustrates the different nature of their sample: these are objects that are already forming massive stars and that have much higher values of L/M. However, we caution that systematic differences could also arise because of the different methods being used to derive masses (i.e., HCO^+ versus mm flux-based masses).

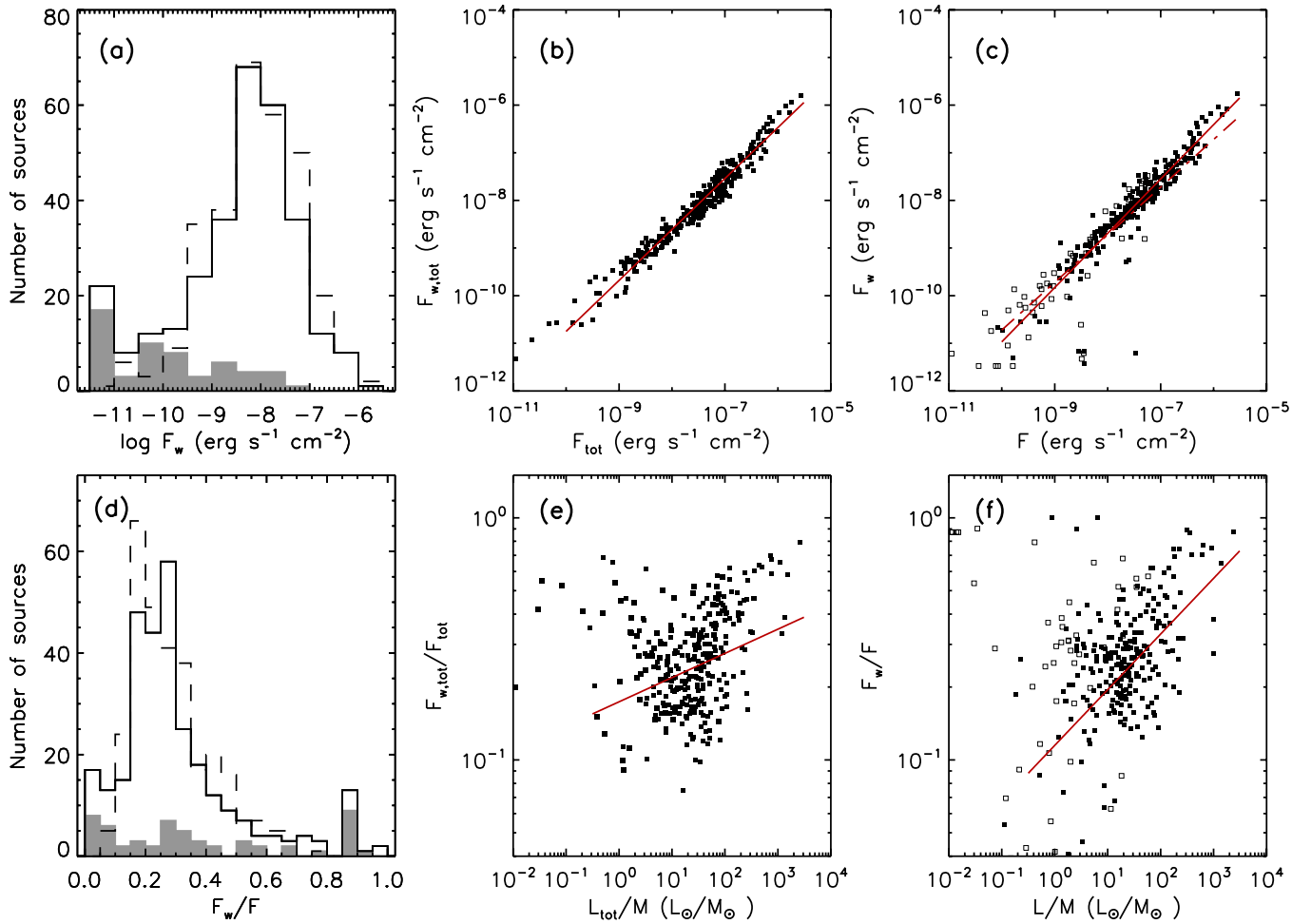

Figure 4. (a) Distributions of F_w (solid line) and $F_{w,\mathrm{tot}}$ (dashed line). The shaded histogram shows the sources for which the bolometric flux, F, measurements are uncertain due to background subtraction (see Figure 2(b)). (b) Correlation of $F_{w,\mathrm{tot}}$ with F_{tot}, with a best-fit relation of $F_{w,\mathrm{tot}} = 0.89 \times F_{\mathrm{tot}}^{1.08}$ with $r_s = 0.98$ and a negligible value of p_s. (c) Correlation of F_w with F, with two best-fit relations shown as $F_{\mathrm{w}} = 2.69(\pm 1.25) \times F^{1.14\pm 0.02}$ (solid line) and $F_{\mathrm{w}} = 0.30(\pm 0.01) \times F$ (dot–dashed line). Open squares show clumps with uncertain measurements of F due to *IRAS* 100 μm background subtraction (see Figure 2(b)). (d) Distribution of F_w/F (solid line) and $F_{w,\mathrm{tot}}/F_{\mathrm{tot}}$ (dashed line), with shaded sources as in (a). (e) Correlation of $F_{w,\mathrm{tot}}/F_{\mathrm{tot}}$ with L_{tot}/M, with best-fit relation $F_{w,\mathrm{tot}}/F_{\mathrm{tot}} = 0.19 \times (L_{\mathrm{tot}}/M/[L_\odot/M_\odot])^{0.10}$ shown with $r_s = 0.29$ and $p_s \ll 10^{-4}$ (formally $p_s = 4.3 \times 10^{-7}$). (f) Correlation of F_w/F with L/M, with best-fit relation $F_{\mathrm{w}}/F = 0.11 \times (L/M/[L_\odot/M_\odot])^{0.23}$ shown with $r_s = 0.43$ and $p_s \ll 10^{-4}$ (formally $p_s = 2.5 \times 10^{-12}$). As star cluster formation proceeds to higher values of L/M, the warmer component becomes more important.

(A color version of this figure is available in the online journal.)

Similarly, Mueller et al. (2002), Beuther et al. (2002), and Faúndez et al. (2004) reported mean values of $\log(L/M)$ as 2.04 ± 0.34, 1.18 ± 0.34, and 1.75 ± 0.38. Note here that in Beuther et al. (2002) they have used opacity from Hildebrand (1983), which is 4.9 times smaller than the opacity from Ossenkopf & Henning (1994) used in Mueller et al. (2002) and Faúndez et al. (2004). So the mass derived in Beuther et al. (2002) would be 4.9 times smaller, and their mean $\log(L/M)$ would be 1.87 ± 0.34 if they adopt the opacity from Ossenkopf & Henning (1994).

4.5. The Warm Component

From the two-temperature fitting process, we derived the total, $F_{\mathrm{w,tot}}$, and background-subtracted, F_w, flux for the warm component. The distributions of $F_{\mathrm{w,tot}}$ and F_w are shown in Figure 4(a). The correlation of $F_{\mathrm{w,tot}}$ with F_{tot} is shown in Figure 4(b), and that of F_w with F in Figure 4(c). These both show significant correlations. We derive a best-fit power-law fit for the dependence of $F_{\mathrm{w,tot}}$ on F_{tot}, finding

$$F_{\mathrm{w,tot}} = 0.89(\pm 0.35) \times F_{\mathrm{tot}}^{1.08\pm 0.02}. \quad (6)$$

For the background subtracted case, which we consider to be the most accurate measure of the intrinsic properties of the clumps, we try two different constrained fits, finding that

$$F_{\mathrm{w}} = 2.69(\pm 1.25) \times F^{1.14\pm 0.02} \quad (7)$$

$$F_{\mathrm{w}} = 0.30(\pm 0.01) \times F. \quad (8)$$

The distributions of $F_{\mathrm{w,tot}}/F_{\mathrm{tot}}$ and F_{w}/F are shown in Figure 4(d). The warm component flux generally accounts for 10%–30% of the total flux, so F_w and F are not independent, which can contribute to these correlations.

To investigate if there are any systematic trends associated with the warm component during star cluster formation as measured by the clump luminosity to mass ratio, we show the correlation of $F_{\mathrm{w,tot}}/F_{\mathrm{tot}}$ versus L_{tot}/M in Figure 4(e) and F_w/F versus L/M in Figure 4(f).

The power-law fit results of this positive correlation are as follows:

$$F_{\mathrm{w,tot}}/F_{\mathrm{tot}} = 0.19(\pm 0.03) \times (L_{\mathrm{tot}}/M/[L_\odot/M_\odot])^{0.10\pm 0.03} \quad (9)$$

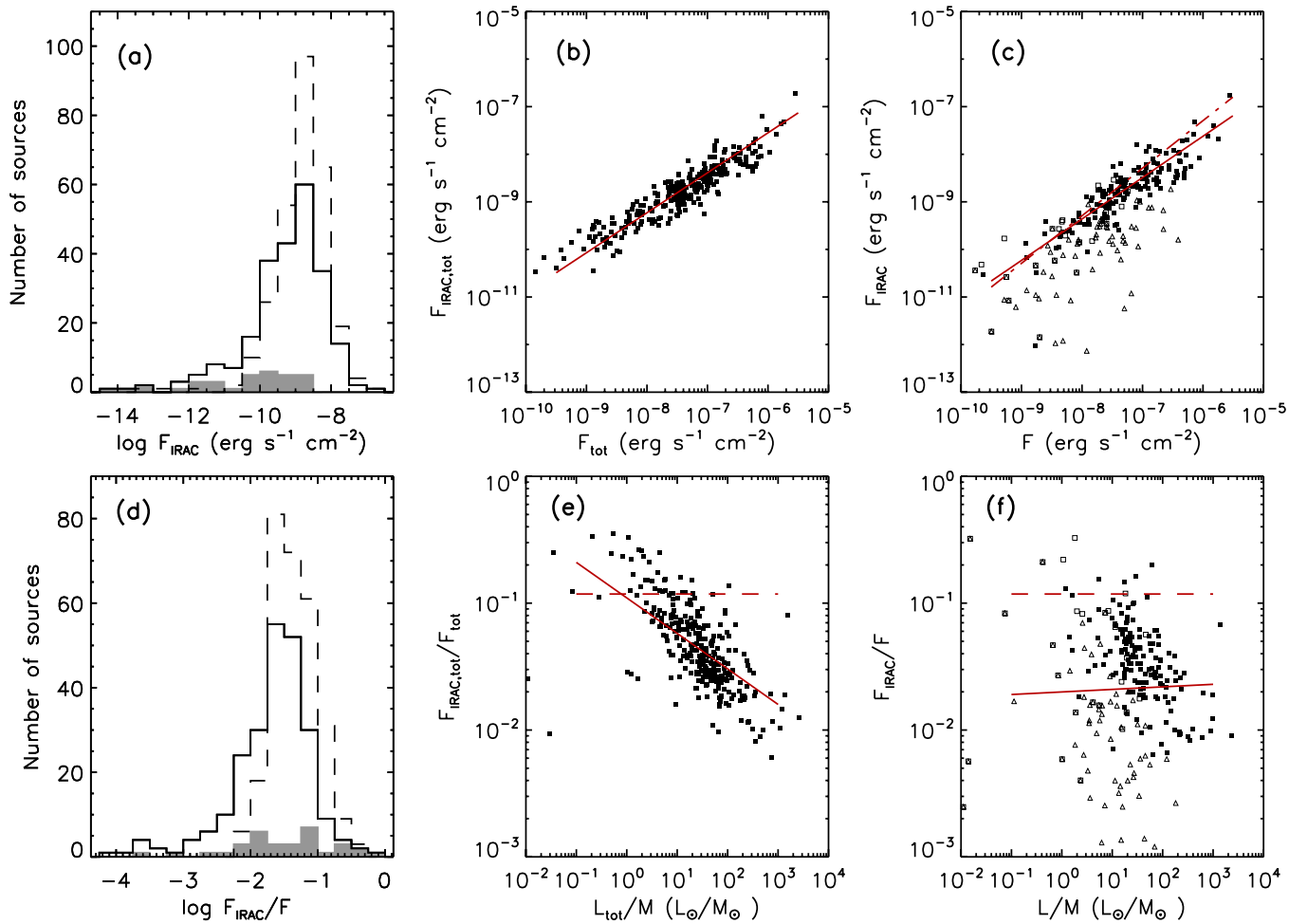

Figure 5. (a) Distributions of $F_{\rm IRAC}$ (solid line) and $F_{\rm IRAC,tot}$ (dashed line). The shaded histogram shows the sources for which the bolometric flux, F, measurements are uncertain due to background subtraction (see Figure 2(b)). (b) Correlation of $F_{\rm IRAC,tot}$ with $F_{\rm tot}$, with a best-fit relation of $F_{\rm IRAC,tot} = 3.1 \times 10^{-3} F_{\rm tot}^{0.84}$. Here $r_s = 0.91$ and p_s is negligible. (c) Correlation of $F_{\rm IRAC}$ with F, with two best-fit relations shown: $F_{\rm IRAC} = 4.0(\pm 3.0) \times 10^{-3} \times F^{0.87\pm0.04}$ (solid line) and $F_{\rm IRAC} = 5.1(\pm 0.6) \times 10^{-2} \times F$ (dot–dashed line). Open squares show clumps with uncertain measurements of F due to *IRAS* 100 μm background subtraction (see Figure 2(b)). Open triangles show clumps with uncertain measurements of $F_{\rm IRAC}$ due to IRAC 8 μm background subtraction. (d) Distribution of $F_{\rm IRAC}/F$ (solid line) and $F_{\rm IRAC,tot}/F_{\rm tot}$ (dashed line), with shaded sources as in panel (a). (e) Correlation of $F_{\rm IRAC,tot}/F_{\rm tot}$ with $L_{\rm tot}/M$, with a best-fit relation of $F_{\rm IRAC,tot}/F_{\rm tot} = 0.11(\pm 0.01) \times (L_{\rm tot}/M/[L_\odot/M_\odot])^{-0.28\pm0.02}$. Here $r_s = -0.69$ and p_s is negligible. The horizontal dashed line corresponds to 0.11, which is the $F_{\rm IRAC}/F$ ratio of the dust emission from the diffuse interstellar medium and is calculated using the data from Li & Draine (2001). (f) Correlation of $F_{\rm IRAC}/F$ with L/M, with a best-fit relation of $F_{\rm IRAC,tot}/F_{\rm tot} = 0.02(\pm 0.002) \times (L/M/[L_\odot/M_\odot])^{0.02\pm0.05}$. Here $r_s = -0.14$ and $p_s = 0.05$, so there is no significant dependence of $F_{\rm IRAC,tot}/F_{\rm tot}$ with L/M.

(A color version of this figure is available in the online journal.)

and

$$F_{\rm w}/F = 0.11(\pm 0.02) \times (L/M/[L_\odot/M_\odot])^{0.23\pm0.02}. \quad (10)$$

The Spearman rank correlation coefficients (see Figure 4) indicates a positive correlation exists in both cases.

Our findings support the idea that as stars gradually form in molecular clumps and the luminosity-to-mass ratio increases, a larger fraction of the bolometric flux will emerge at shorter wavelengths. The specific functional form of this correlation is a constraint on radiative transfer models of star cluster formation.

4.6. The Hot (IRAC Band) Component

We now search for any correlation of the IRAC band flux, which extends from ∼3–9 μm, with the bolometric flux and the luminosity to mass. These relatively short wavelengths are more sensitive to hot dust directly heated by embedded young stars. We first measure the total IRAC band flux using a simple trapezoidal rule integration in the four IRAC bands, without background subtraction, $F_{\rm IRAC,tot}$, and then subtract the background to derive $F_{\rm IRAC}$.

The distributions of $F_{\rm IRAC,tot}$ and $F_{\rm IRAC}$ are shown in Figure 5(a). The correlation of $F_{\rm IRAC,tot}$ with $F_{\rm tot}$ is shown in Figure 5(b) and that of $F_{\rm IRAC}$ with F in Figure 5(c). These both show highly significant correlations. The power-law fit results of these two correlations are as follows:

$$F_{\rm IRAC,tot} = 3.1(\pm 1.7) \times 10^{-3} \times F_{\rm tot}^{0.84\pm0.03} \quad (11)$$

and, trying two constrained fits,

$$F_{\rm IRAC} = 4.0(\pm 3.0) \times 10^{-3} \times F^{0.87\pm0.04} \quad (12)$$

$$F_{\rm IRAC} = 5.1(\pm 0.6) \times 10^{-2} \times F. \quad (13)$$

The distributions of $F_{\rm IRAC,tot}/F_{\rm tot}$ and $F_{\rm IRAC}/F$ are shown in Figure 5(d). The IRAC component flux generally accounts

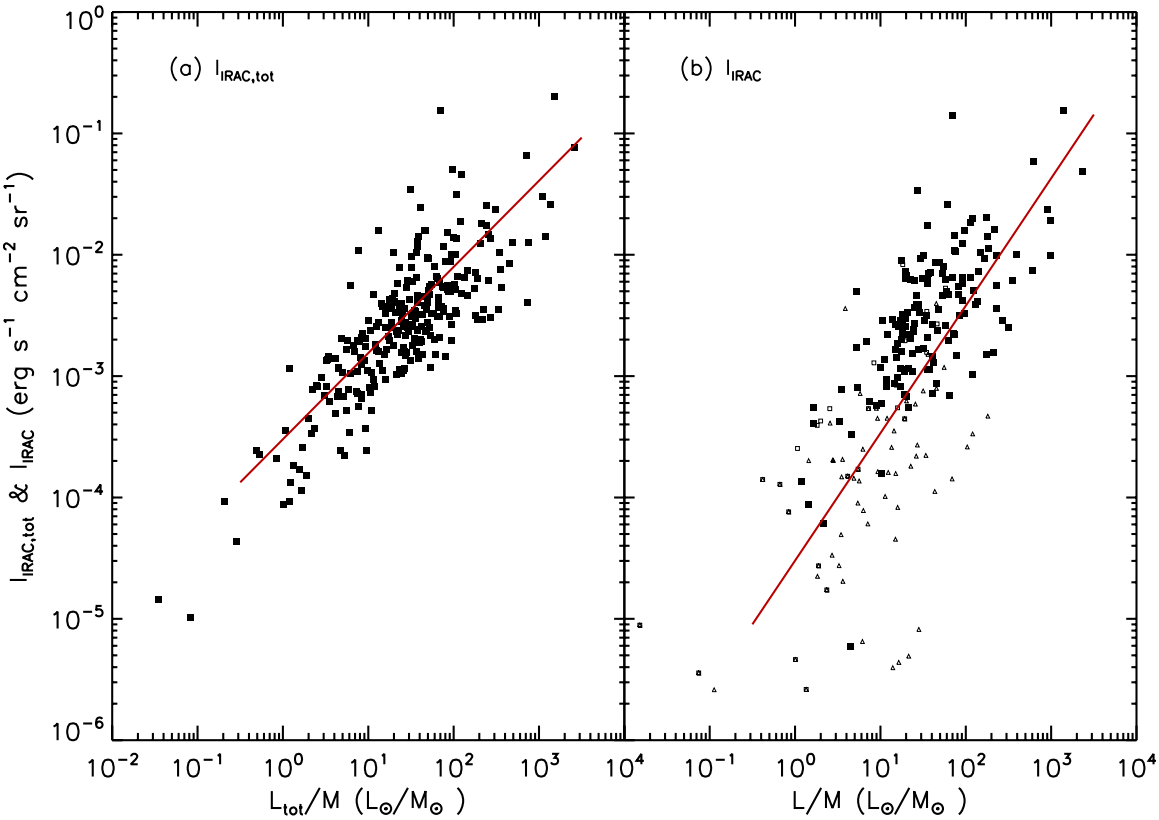

Figure 6. (a) Correlation of $I_{\rm IRAC,tot}$ with $L_{\rm tot}/M$, with a best-fit relation of $I_{\rm IRAC,tot} = 3.0(\pm 0.5) \times 10^{-4} \times (L_{\rm tot}/M/[L_\odot/M_\odot])^{0.71(\pm 0.05)}$ with $r_s = 0.57$ and a negligible value of p_s. (b) Correlation of $I_{\rm IRAC}$ with L/M, with a best-fit relation of $I_{\rm IRAC} = 3.0(\pm 0.7) \times 10^{-5} \times (L/M/[L_\odot/M_\odot])^{1.05(\pm 0.05)}$ with $r_s = 0.66$ and a negligible value of p_s. Open squares show clumps with uncertain measurements of F due to *IRAS* 100 μm background subtraction (see Figure 2(b)). Open triangles show clumps with uncertain measurements of $F_{\rm IRAC}$ due to IRAC 8 μm background subtraction.

(A color version of this figure is available in the online journal.)

for ∼1%–10% of the total flux, so $F_{\rm IRAC}$ and F are essentially independent, unlike for F_w (above).

To investigate if there are any systematic trends associated with the IRAC (hot) component during star cluster formation as measured by the clump luminosity to mass ratio, we show the correlation of $F_{\rm IRAC,tot}/F_{\rm tot}$ versus $L_{\rm tot}/M$ in Figure 5(e) and $F_{\rm IRAC}/F$ versus L/M in Figure 5(f). The best-fit power-law relations are as follows:

$$F_{\rm IRAC,tot}/F_{\rm tot} = 0.11(\pm 0.01) \times (L_{\rm tot}/M/[L_\odot/M_\odot])^{-0.28\pm 0.02}. \quad (14)$$

The Spearman rank correlation coefficient of $F_{\rm IRAC,tot}/F_{\rm tot}$ versus $L_{\rm tot}/M$ is negative. We expect this is due to the fact that $F_{\rm tot}$ and $L_{\rm tot}$ are correlated, while $F_{\rm IRAC,tot}$ is often dominated by "background" (i.e., both background and foreground, i.e., unrelated) emission.

Attempting a power-law fit for $F_{\rm IRAC}/F$ versus L/M, we find

$$F_{\rm IRAC}/F = 0.02(\pm 0.002) \times (L/M/[L_\odot/M_\odot])^{0.02\pm 0.05}, \quad (15)$$

but with $r_s = -0.14$ and $p_s = 0.05$, indicating that there is no significant correlation. Thus there is no evidence for an increase in the relative importance of the hot component as cluster evolution (as measured by L/M) proceeds. As the luminosity input into the clump rises, a fairly constant fraction emerges in the IRAC bands. Again, this result can provide a constraint on theoretical models of star cluster formation.

In order to more directly probe the evolution of IRAC-traced hot dust emission and its possible correlation with luminosity-to-mass ratio, we also calculated the IRAC band-specific intensity (surface brightness) without, $I_{\rm IRAC,tot}$ and with, $I_{\rm IRAC}$ background subtraction (Figure 6). Note that both the specific intensities and the luminosity-to-mass ratios are essentially independent of distance uncertainties. The best-fit relations are as follows:

$$I_{\rm IRAC,tot} = 3.0(\pm 0.5) \times 10^{-4} \times (L_{\rm tot}/M/[L_\odot/M_\odot])^{0.71(\pm 0.05)}\ {\rm erg\ s^{-1}\ cm^{-2}\ sr^{-1}} \quad (16)$$

with $r_s = 0.57$ and $p_s \ll 10^{-4}$ (formally $p_s = 10^{-13}$), and, trying two constrained fits,

$$I_{\rm IRAC} = 3.0(\pm 0.7) \times 10^{-5} \times (L/M/[L_\odot/M_\odot])^{1.05(\pm 0.05)}\ {\rm erg\ s^{-1}\ cm^{-2}\ sr^{-1}} \quad (17)$$

$$I_{\rm IRAC} = 5.0(\pm 1.9) \times 10^{-5} \times (L/M/[L_\odot/M_\odot])\ {\rm erg\ s^{-1}\ cm^{-2}\ sr^{-1}}. \quad (18)$$

The former has $r_s = 0.66$ and $p_s \ll 10^{-4}$ (formally p_s=10^{-19}).

Thus the IRAC band-specific intensity, which is essentially independent of L/M (since only a very small fraction of L emerges at these wavelengths) and more directly traces embedded stellar populations, has a significant correlation with L/M, thus validating the use of L/M as an evolutionary indicator of star cluster formation. The specific functional form of the correlation is a constraint on radiative transfer models of star cluster formation.

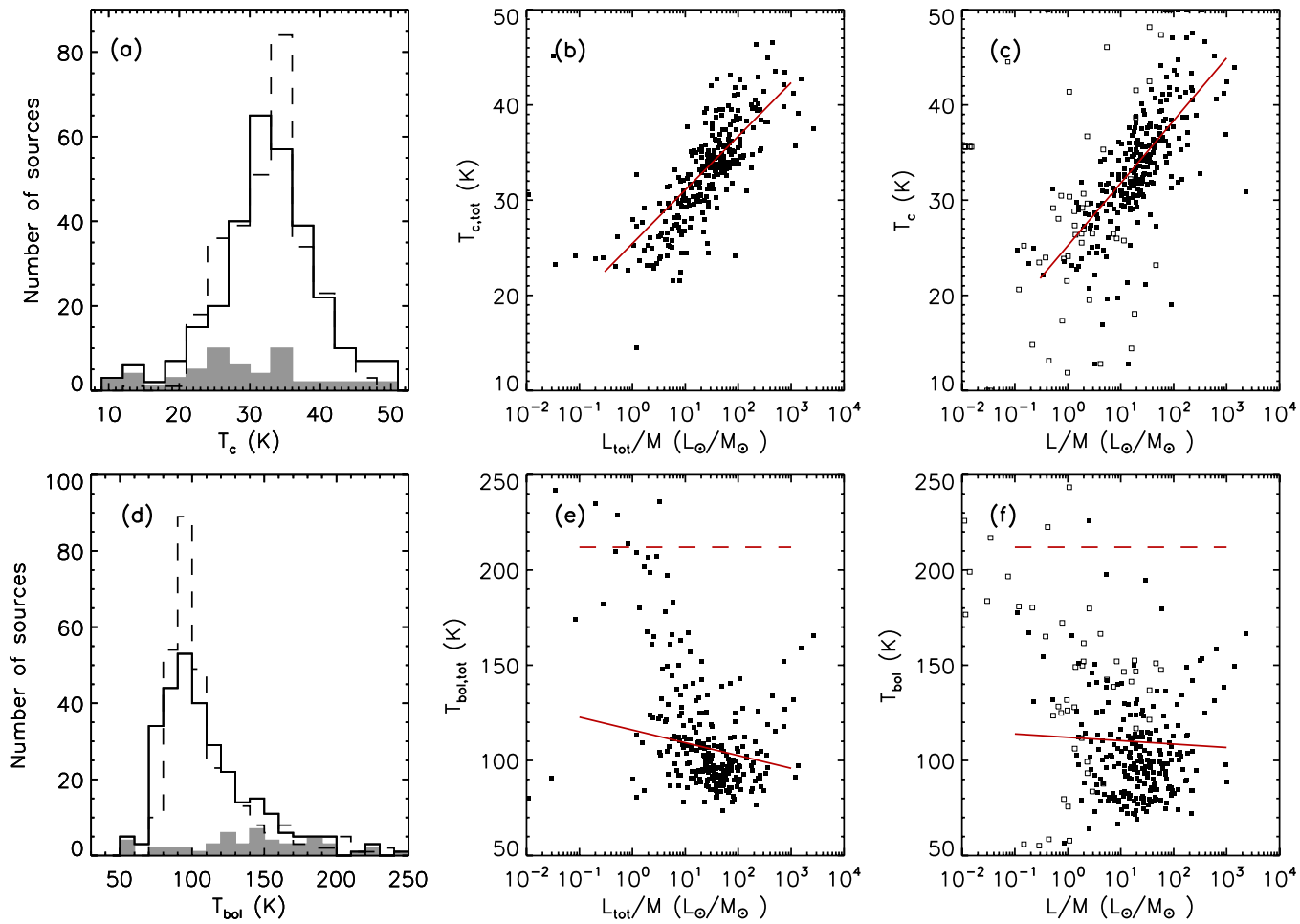

Figure 7. (a) Distribution of T_c (solid line) and $T_{c,\rm tot}$ (dashed line). The shaded histogram shows the sources for which the bolometric flux, F, measurements are uncertain due to background subtraction (see Figure 2). (b) Correlation of $T_{c,\rm tot}$ with $L_{\rm tot}/M$, with a best-fit relation of $T_{c,\rm tot}/{\rm K} = 5.6(\pm0.5)\times\log(L_{\rm tot}/M/[L_\odot/M_\odot])+25.4(\pm0.8)$, $r_s = 0.81$ and a negligible value of p_s. (c) Correlation of T_c with L/M, with a best-fit relation of $T_c/{\rm K} = 6.6(\pm0.6) \times \log(L/M/[L_\odot/M_\odot]) + 25.2(\pm1.0)$ with $r_s = 0.65$ and $p_s = 4.8 \times 10^{-38}$. Open squares show clumps with uncertain measurements of F due to *IRAS* 100 μm background subtraction (see Figure 2(b)). (d) Distribution of $T_{\rm bol}$ (solid line) and $T_{\rm bol,tot}$ (dashed line). The shaded histogram shows the sources for which the bolometric flux, F, measurements are uncertain due to background subtraction (see Figure 2). (e) $T_{\rm bol,tot}$ vs. $L_{\rm tot}/M$, which does not show a significant correlation (the best-fit relation of $T_{\rm bol,tot}/{\rm K} = -6.7(\pm3.4) \times \log(L_{\rm tot}/M/[L_\odot/M_\odot]) + 116.0(\pm6.4)$ has $r_s = -0.15$ and $p_s = 0.06$). The horizontal dashed line represents $T = 210$ K, which is the bolometric temperature of the dust emission in the diffuse ISM calculated using the data from Li & Draine (2001). (f) $T_{\rm bol}$ vs. L/M, which also does not show a significant correlation (the best-fit relation of $T_{\rm bol}/{\rm K} = -1.8(\pm3.3) \times \log(L/M/[L_\odot/M_\odot]) + 112.1(\pm3.3)$ has $r_s = -0.15$ and $p_s = 0.06$).

(A color version of this figure is available in the online journal.)

The near linear relation of $I_{\rm IRAC}$ with L/M (although with large scatter, which may be expected from IMF sampling) suggests that $I_{\rm IRAC}$ also has a near linear dependence on embedded stellar content relative to gas mass, i.e., the instantaneous star formation efficiency, $\epsilon' \equiv M_*/M$, which, note, is normalized by the gas mass. (We define $\epsilon \equiv M_*/(M_*+M)$, which becomes similar to ϵ' when $\epsilon' \ll 1$.) Thus, for a Salpeter IMF down to 0.1 $M_\odot$ (see Section 4.4),

$$\epsilon' \simeq 1.0\frac{L/M}{600L_\odot/M_\odot} \simeq 0.33(\pm0.16)\frac{I_{\rm IRAC}}{10^{-2}\ {\rm erg\ s^{-1}\ cm^{-2}\ sr^{-1}}}, \quad (19)$$

where we have used the numerical result of the constrained linear fit (Equation (18)). This may be a useful relation for estimating star formation efficiencies of statistical samples of star-forming clumps (at least those with similar densities to local Galactic clumps), when only IRAC data are available and a background subtraction can be performed.

4.7. Cold Component Dust Temperature and Bolometric Temperature

We now search for any dependence of the cold-component dust temperature, $T_{c,\rm tot}$ (based on total fluxes with no background subtracted) and T_c (based on fluxes after background subtraction), with the luminosity-to-mass ratio. We note that the available data for the clumps generally are limited at long wavelengths to the *IRAS* 100 μm data and so our accuracy for estimating T_c is limited to about ±5 K (see Section 3.2).

The distributions of $T_{c,\rm tot}$ and T_c are shown in Figure 7(a). The mean values are $\langle T_{c,\rm tot}\rangle = 33 \pm 5$ K and $\langle T_c\rangle = 33 \pm 7$ K. These results are similar to those derived in other surveys, such as $\langle T\rangle = 29 \pm 9$ K in the large sample of Mueller et al. (2002); $\langle T\rangle = 45 \pm 11$ K in the large sample of Sridharan et al. (2002); $\langle T\rangle = 32 \pm 5$ K in the sample of Molinari et al. (2000); $\langle T\rangle = 35\pm6$ K in the sample of Hunter et al. (2000); $\langle T\rangle = 30$ K in the sample of Molinari et al. (2008); and $\langle T\rangle = 32$ K in the sample of Faúndez et al. (2004).

The correlation of $T_{c,\rm tot}$ with $L_{\rm tot}/M$ is shown in Figure 7(b) and that of $T_{\rm c}$ with L/M in Figure 7(c). We see that clear positive correlations are present—the temperature rises as L/M increases. We find the following best-fit relations:

$$T_{c,\rm tot}/{\rm K} = 5.6(\pm 0.5) \times \log(L_{\rm tot}/M/[L_\odot/M_\odot]) + 25.4(\pm 0.8) \quad (20)$$

with $r_s = 0.81$ and a negligible value of p_s, and

$$T_c/{\rm K} = 6.6(\pm 0.6) \times \log(L/M/[L_\odot/M_\odot]) + 25.2(\pm 1.0) \quad (21)$$

with $r_s = 0.65$ and a negligible value of p_s.

"Bolometric temperature," $T_{\rm bol}$, has been proposed as a measure of the evolutionary development of a YSO (Ladd et al. 1991; Myers & Ladd 1993; Myers et al. 1998). It is the temperature of a black body having the same weighted mean frequency as the observed SED. As the envelopes in YSO systems are dispersed, their bolometric temperatures will rise. This is because the FIR emission decreases while the NIR and MIR emission increases.

We calculated the bolometric temperature for our molecular clumps following Myers & Ladd (1993):

$$T_{\rm bol} = 1.25 \times 10^{-11} \langle \nu \rangle \ \ {\rm K\,Hz^{-1}}, \quad (22)$$

where $\langle \nu \rangle \equiv \int_0^\infty \nu F_\nu d\nu / \int_0^\infty F_\nu d\nu$ is the flux-weighted mean frequency. The coefficient of $\langle \nu \rangle$ in Equation (22) is chosen so that a black-body emitter at temperature T has $T_{\rm bol} = T$.

The distributions of $T_{\rm bol,tot}$ (based on total fluxes with no background subtraction) and $T_{\rm bol}$ (based on fluxes after background subtraction) are shown in Figure 7(d). These have mean values of 92 ± 18 K and 113 ± 44 K, respectively. For comparison, Mueller et al. (2002) find a mean value of 78 ± 21 K for their sample.

The correlation of $T_{\rm bol,tot}$ with $L_{\rm tot}/M$ is shown in Figure 7(e) and that of $T_{\rm bol}$ with L/M in Figure 7(f). We do not find significant correlations, since the best-fit relations are

$$T_{\rm bol,tot}/{\rm K} = -6.7(\pm 3.4) \times \log(L_{\rm tot}/M/[L_\odot/M_\odot]) + 116.0(\pm 6.4) \quad (23)$$

with $r_s = -0.15$ and $p_s = 0.06$, and

$$T_{\rm bol}/{\rm K} = -1.8(\pm 3.3) \times \log(L/M/[L_\odot/M_\odot]) + 112.1(\pm 3.3) \quad (24)$$

with $r_s = -0.15$ and $p_s = 0.06$. We suspect that the lack of significant correlation is because the uncertainties in deriving $T_{\rm bol}$ are relatively large compared to the expected size of any trend for $T_{\rm bol}$ to increase during star cluster formation. This is in contrast to the measures F_w/F and $I_{\rm IRAC}$, which show clear changes by about a factor of 10 or more as L/M increases.

5. DISCUSSION

5.1. Dependence of L and L/M on Mass Surface Density, Σ

Consider a clump that forms stars at a fixed efficiency per free-fall time, $\epsilon_{\rm ff}$. The overall accretion rate to stars is

$$\dot{M}_* = \epsilon_{\rm ff} \frac{M}{t_{\rm ff}} = \frac{(8G)^{1/2}}{\pi^{1/4}} \epsilon_{\rm ff} (M\Sigma)^{3/4} = 2.92 \times 10^{-4} \frac{\epsilon_{\rm ff}}{0.02} \left(\frac{M}{10^3\ M_\odot} \frac{\Sigma}{{\rm g\ cm^{-2}}} \right)^{3/4} M_\odot\ {\rm yr}^{-1}, \quad (25)$$

where we have normalized to a value of $\epsilon_{\rm ff}$ estimated by Krumholz & Tan (2007). Then the accretion luminosity is

$$L_{\rm acc} = f_{\rm acc} \frac{G\dot{M}_* \bar{m}_*}{\bar{r}_*} = 2270 f_{\rm acc} \frac{\bar{m}_*}{M_\odot} \frac{4R_\odot}{\bar{r}_*} \frac{\epsilon_{\rm ff}}{0.02} \left(\frac{M}{10^3\ M_\odot} \frac{\Sigma}{{\rm g\ cm^{-2}}} \right)^{3/4} L_\odot. \quad (26)$$

Here $f_{\rm acc}$ is the fraction of the accretion power that is radiated. While for individual protostars we expect $f_{\rm acc} \sim 0.5$ because of the mechanical luminosity of protostellar outflows, in early-stage star-forming clumps much of the outflow kinetic energy is likely to be liberated via radiative shocks and thus contribute to the total clump luminosity. Thus we adopt $f_{\rm acc} = 1$ as a fiducial value. In the above equation, $\bar{m}_*$ is the mean protostellar mass, weighted by an accretion energy release. For a Salpeter IMF from 0.1 to 120 $M_\odot$, the mean stellar mass is 0.353 $M_\odot$, while the mean gravitational energy is $2.06 G M_\odot^2/\bar{r}_*$, assuming $\bar{r}_*$ is independent of m_* (discussed below). For accretion near the end of individual star formation, this implies $\bar{m}_* \simeq 1.4\ M_\odot$; however the typical unit of accretion energy release will be when the protostar has $2^{-1/2}$ of its final mass. Thus we estimate $\bar{m}_* \simeq 1\ M_\odot$ as a typical fiducial value in Equation (26).

The protostellar evolution models of Tan & McKee (2002), developed for protostars forming with accretion rates appropriate for cores fragmenting from a clump with $\Sigma \simeq 1$ g cm^{-2} (see also Stahler 1988; Palla & Stahler 1992; Nakano et al. 2000; McKee & Tan 2003), indicate that the sizes of all protostars are close to ~ 3 to 4 $R_\odot$ when their masses are $\lesssim 1\ M_\odot$. After this the size increases along the deuterium core burning sequence, reaching about 6 $R_\odot$ by the time the protostars have 1.5 $M_\odot$. After this, sizes stay relatively constant until $m_* \sim 5\ M_\odot$. Given these relatively modest changes in r_* with m_*, we adopt a fiducial value of $\bar{r}_* = 4\ R_\odot$ in Equation (26).

We can now use Equations (26) and (3) to estimate minimum values of L/M for star-forming clumps. We have

$$\frac{L_{\rm min}/M}{L_\odot/M_\odot} = 0.77 \left(\frac{T}{15\ {\rm K}} \right)^{5.65} + \frac{L_{\rm acc}/M}{L_\odot/M_\odot} \quad (27)$$

$$= 0.77 \left(\frac{T}{15\ {\rm K}} \right)^{5.65} + 2.27 f_{\rm acc} \frac{\bar{m}_*}{M_\odot} \frac{4R_\odot}{\bar{r}_*} \frac{\epsilon_{\rm ff}}{0.02} \times \left(\frac{M}{10^3\ M_\odot} \right)^{-1/4} \left(\frac{\Sigma}{{\rm g\ cm^{-2}}} \right)^{3/4}, \quad (28)$$

where T is the dust temperature expected from ambient heating of starless clumps. Note that because of internal stellar luminosities that will contribute in addition to $L_{\rm acc}$, $L_{\rm min}/M$ provides only a lower bound on the distribution of L/M of star-forming clumps.

In Figures 8(a) and (b), we plot the dependence of $L_{\rm tot}$ and L with Σ. Note Σ, like M, is based on the HCO^+ observations and analysis. We estimate Σ as $M/2$ divided by the projected area of the FWHM ellipse of Paper I. This will give a value of Σ for the typical mass element in the clump. We find the following best-fit relations:

$$L_{\rm tot} = 3.15(\pm 1.33) \times 10^5 \times (\Sigma/{\rm g\ cm^{-2}})^{1.03 \pm 0.15}\ L_\odot \quad (29)$$

with $r_s = 0.33$ and $p_s \ll 10^{-4}$ (formally $p_s = 6 \times 10^{-9}$), and

$$L = 1.70(\pm 0.76) \times 10^5 \times (\Sigma/{\rm g\ cm^{-2}})^{0.70 \pm 0.18}\ L_\odot \quad (30)$$

with $r_s = 0.34$ and $p_s \ll 10^{-4}$ (formally $p_s = 2 \times 10^{-9}$).

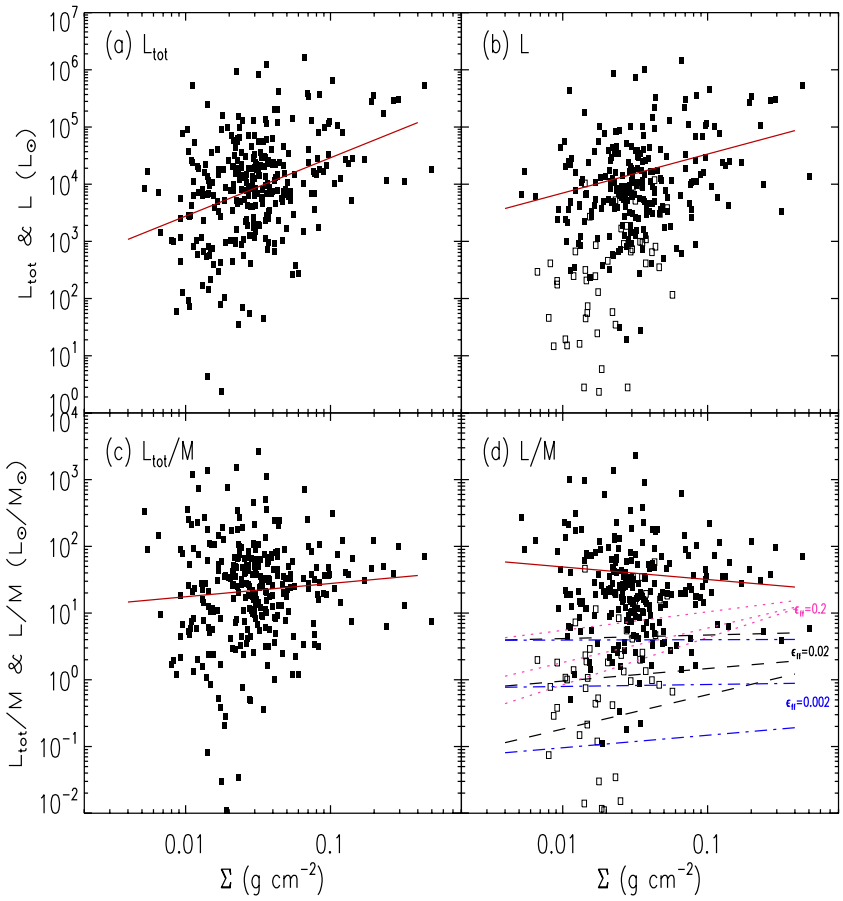

Figure 8. (a) Correlation of $L_{\rm tot}$ with clump mass surface density Σ. The solid line shows the best-fit relation (see text). (b) Correlation of L with Σ. The solid line shows the best-fit relation (see the text). The open squares show clumps with uncertain measurements of F due to *IRAS* 100 μm background subtraction (see Figure 2(b)). (c) Correlation of $L_{\rm tot}/M$ with Σ. The solid line shows the best-fit relation (see text). (d) Correlation of L/M with Σ. The solid line shows the best-fit relation (see the text). The three (black) dashed lines show the minimum $L_{\rm min}/M$ expected from only ambient heating and accretion luminosity for clumps $M = 10^3\ M_\odot$, $T = 10, 15, 20$ K (from bottom to top) forming stars at fixed $\epsilon_{\rm ff} = 0.02$ (Equation (28)). The three (blue) dash–dotted lines show the minimum $L_{\rm min}/M$ with mass $10^3\ M_\odot$, $T = 10, 15, 20$ K (from bottom to top) forming stars at $\epsilon_{\rm ff} = 0.002$. The three (magenta) dotted lines show the minimum $L_{\rm min}/M$ with mass $10^3\ M_\odot$, $T = 10, 15, 20$ K (from bottom to top) forming stars at $\epsilon_{\rm ff} = 0.2$. The open squares show clumps with uncertain measurements of F due to *IRAS* 100 μm background subtraction (see Figure 2(b)). (A color version of this figure is available in the online journal.)

In Figures 8(c) and (d), we plot the dependence of $L_{\rm tot}/M$ and L/M with Σ. We do not find any evidence for a correlation, since the best-fit relations are

$$L_{\rm tot}/M = 44.1(\pm 17.0) \times (\Sigma/{\rm g\ cm^{-2}})^{0.20\pm0.14}\ L_\odot/M_\odot \quad (31)$$

with $r_s = 0.07$ and $p_s = 0.26$, and

$$L/M = 20.4(\pm 5.5) \times (\Sigma/{\rm g\ cm^{-2}})^{-0.19\pm0.14}\ L_\odot/M_\odot \quad (32)$$

with $r_s = -0.12$ and $p_s = 0.14$.

One caveat of the above results is that L/M and Σ are inversely correlated via M, and this may be making it more difficult to discern any rise of L/M with Σ. We note that high Σ clumps, e.g., those with $\Sigma > 0.1$ g cm^{-2} all have $L/M \gtrsim 4 L_\odot/M_\odot$. We also considered our other "good" cluster evolution indicators, F_w/F, $I_{\rm IRAC}$ and T_c and their dependence on Σ. However, we did not find any significant correlations of these properties with Σ.

In Figure 8(d), we also show the predictions of Equation (28) for clumps with $M = 10^3\ M_\odot$, $T = 10, 15, 20$ K forming stars at fixed $\epsilon_{\rm ff} = 0.002, 0.02, 0.2$. Models with $T \sim 10$–15 K appear to define the lower boundary of the populated region of the observed L/M versus Σ parameter space, but obtaining precise constraints on $\epsilon_{\rm ff}$ is difficult because of the sensitivity of L/M to the adopted temperature. The models with high values of $\epsilon_{\rm ff} = 0.2$, even with $T = 10$ K appear to exceed the observed L/M of a significant number of the clumps, thus we tentatively conclude that $\epsilon_{\rm ff} < 0.2$. This analysis will be improved once FIR data become available, allowing individual clump temperatures to be accurately measured from their SEDs. The implications of the detailed distribution of L/M of the clump population and its implication for star cluster formation theories will be examined in a future article.

5.2. Dependence of L and L/M with Velocity Dispersion and Virial Parameter

In Figures 9(a) and (b), we explore the dependence of $L_{\rm tot}$ and L on the one-dimensional velocity dispersion, σ, (as measured from HCO^+(1–0) in Paper I). We find the following best-fit relations:

$$L_{\rm tot} = 11300(\pm 1900) \times (\sigma/{\rm km\ s^{-1}})^{1.09\pm0.26}\ L_\odot \quad (33)$$

with $r_s = 0.28$ and $p_s \ll 10^{-4}$ (formally $p_s = 6.8 \times 10^{-6}$), and

$$L = 7400(\pm 1200) \times (\sigma/{\rm km\ s^{-1}})^{1.14\pm0.28}\ L_\odot \quad (34)$$

with $r_s = 0.26$ and $p_s \lesssim 10^{-4}$ (formally $p_s = 3.2 \times 10^{-5}$). We expect that σ correlates with M for clumps that are

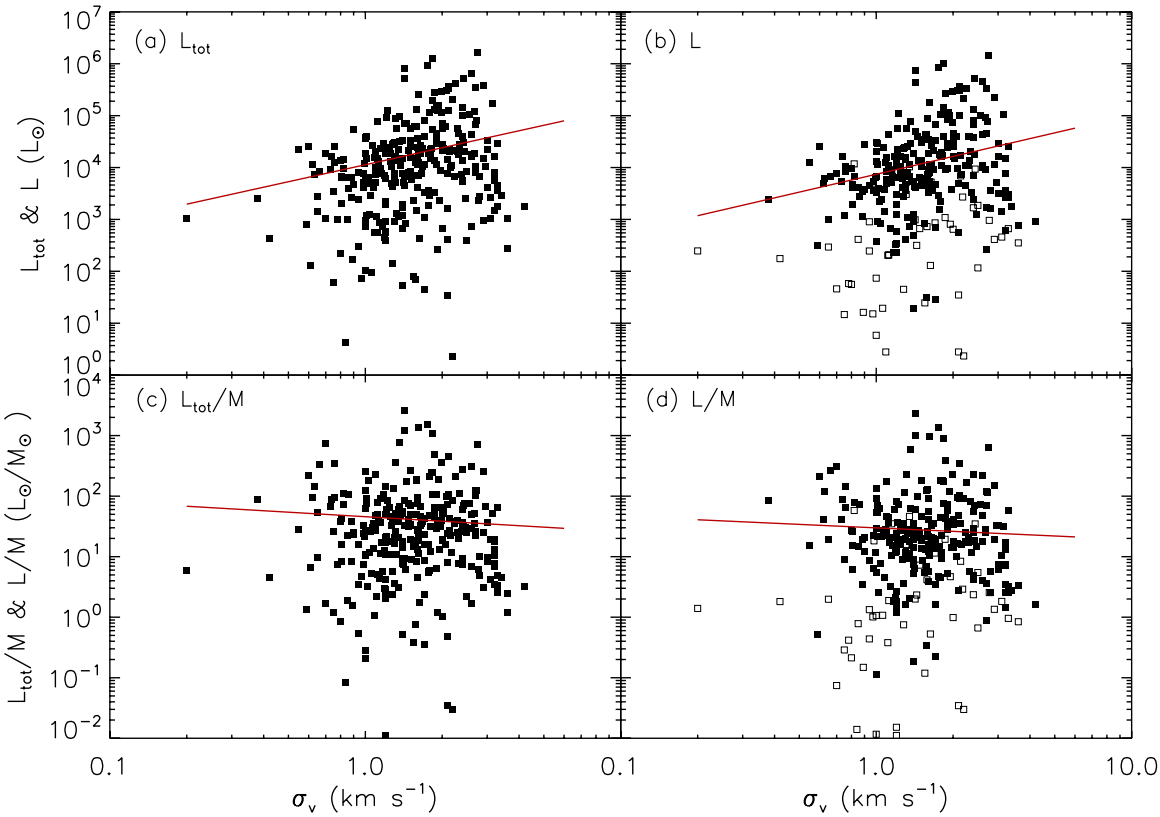

Figure 9. (a) Correlation of L_{tot} with σ_v. The solid line shows the best-fit relation (see the text). (b) Correlation of L with σ_v. The solid line shows the best-fit relation (see text). (c) Correlation of L_{tot}/M with σ_v. The solid line shows the best-fit relation (see the text). (d) Correlation of L/M with σ_v. The solid line shows the best-fit relation (see the text). Open squares show clumps with uncertain measurements of F due to *IRAS* 100 μm background subtraction (see Figure 2(b)).

(A color version of this figure is available in the online journal.)

self-gravitating. Since L correlates with M, this can explain the observed weaker correlation of L with σ.

Similarly, in Figures 9(c) and (d) we show the dependence of L_{tot}/M and L/M with σ. We do not find significant correlations, since the best-fit relations are

$$L_{tot}/M = 46(\pm 6) \times (\sigma/\mathrm{km\ s^{-1}})^{-0.25\pm0.23}\ L_\odot/M_\odot \qquad (35)$$

with $r_s = -0.05$ and $p_s = 0.41$, and

$$L/M = 30(\pm 4) \times (\sigma/\mathrm{km\ s^{-1}})^{-0.19\pm0.24}\ L_\odot/M_\odot \qquad (36)$$

with $r_s = -0.04$ and $p_s = 0.46$. Thus there is no apparent correlation of these variables. If star clusters were built-up hierarchically from a merger of smaller clumps, one might have expected to see increasing L/M with σ.

The virial parameter, $\alpha_{vir} \equiv 5\sigma^2 R/(GM)$ (Bertoldi & McKee 1992), is proportional to the ratio of a clump's kinetic and gravitational energies. In Figures 10(a) and (b), we show the dependence of L_{tot} and L with α_{vir}. We find the following best-fit relations:

$$L_{tot} = 52000(\pm 15000) \times (\alpha_{vir})^{-0.55\pm0.14}\ L_\odot \qquad (37)$$

with $r_s = -0.24$ and $p_s = 1 \times 10^{-4}$, and

$$L = 39000(\pm 12000) \times (\alpha_{vir})^{-0.60\pm0.15}\ L_\odot \qquad (38)$$

with $r_s = -0.27$ and $p_s \lesssim 10^{-4}$ (formally $p_s = 2 \times 10^{-5}$). These (only moderately) significant correlations may be explained by the fact that smaller virial parameters indicate more gravitationally bound systems, which should be more prone to star formation. However, these relations may alternatively be driven by the fact that more massive clumps tend to have smaller virial parameters (Bertoldi & McKee 1992; Paper I) and that luminosity correlates with mass (Section 4.4).

This second explanation appears to be supported by the following results. In Figures 10(c) and (d) we show the dependence of L_{tot}/M and L/M with α_{vir} (note, these are equivalent to correlating L_{tot} and L with $\sigma^2 R$). We do not find significant correlations as the best-fit relations are

$$L_{tot}/M = 29(\pm 8) \times (\alpha_{vir})^{0.18\pm0.12}\ L_\odot/M_\odot \qquad (39)$$

with $r_s = 0.06$ and $p_s = 0.36$, and

$$L/M = 22(\pm 6) \times (\alpha_{vir})^{0.12\pm0.13}\ L_\odot/M_\odot \qquad (40)$$

with $r_s = 0.009$ and $p_s = 0.89$. Thus these data do not reveal any correlation of cluster evolutionary stage (as measured by L/M) with degree of gravitational boundedness.

Note that the absolute values of α_{vir} appear relatively high, e.g., compared to the somewhat larger ^{13}CO clouds and clumps analyzed by Roman-Duval et al. (2010), which have $\bar{\alpha}_{vir} \sim 1$ (see also Tan et al. 2013). As discussed above (Section 3.1), potential systematic uncertainties, especially in the measurement of mass via an assumed HCO^+ abundance, may be causing an overestimation of α_{vir}, but these uncertainties are not expected to lead to a median value of the HCO^+ clump sample that is close to unity. Thus the dynamics of the HCO^+ clumps may be dominated by surface pressure, rather than by their self-gravity (see also Paper I). This is consistent with the fact that most of the

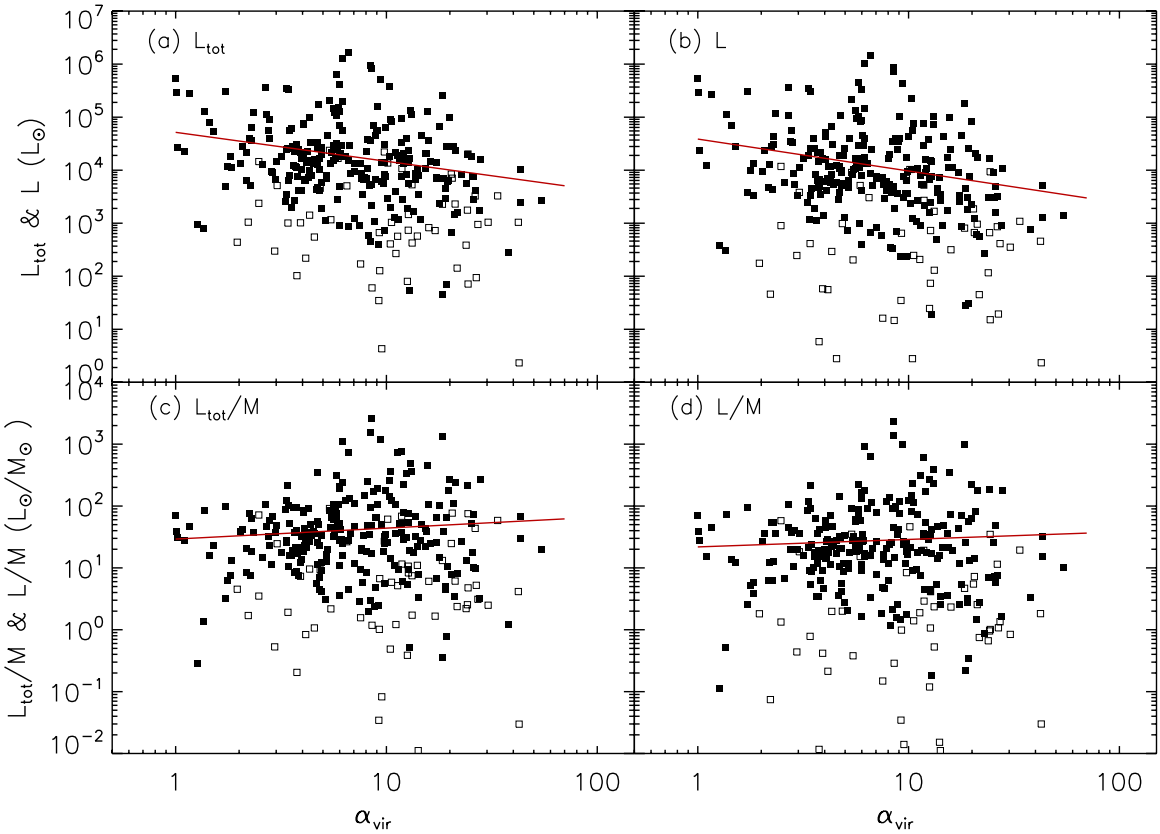

Figure 10. (a) Correlation of virial parameter α with $L_{\rm tot}$. The solid line shows the best-fit relation (see the text). (b) Correlation of virial parameter α with L. The solid line shows the best-fit relation (see the text). (c) Correlation of virial parameter α with $L_{\rm tot}/M$. The solid line shows the best-fit relation (see the text). (d) Correlation of virial parameter α with L/M. The solid line shows the best-fit relation (see the text). The open squares show clumps with uncertain measurements of F due to *IRAS* 100 μm background subtraction (see Figure 2(b)).

(A color version of this figure is available in the online journal.)

HCO^+ clumps have relatively low L/M and low star formation activity, so we may expect them to have values of $\alpha_{\rm vir}$ in the range of ∼1–30, similar to results found by Bertoldi & McKee (1992).

However, it is interesting that we do not see a trend of decreasing $\alpha_{\rm vir}$ with increasing L/M. Possible explanations are as follows: (1) the uncertainties in $\alpha_{\rm vir}$ (which depends on M, R, and σ^2) and L/M are large enough to wash-out any correlation that is present; (2) the importance of self-gravity, as measured at the HCO^+ clump scale, does not grow during star cluster formation. Improved mass, luminosity, and velocity dispersion measurements are needed to investigate this issue further.

5.3. Dependence of L with HCO^+(1–0) Line Luminosity

Gao & Solomon (2004) found a tight linear correlation between the infrared luminosity (hereafter we refer to this as the bolometric luminosity, L) and the amount of dense gas as traced by the luminosity of HCN in both normal galaxies and starburst galaxies. This may suggest that the SFR (thought to be proportional to L, at least in starbursts) simply scales with the mass of dense gas. Similarly, Juneau et al. (2009) found an index of 0.99 ± 0.26 in their study of the relation between the bolometric luminosity and HCO^+ line luminosity in a sample of 34 nearby galaxies.

On the much smaller scales of clumps, the luminosity should not be such a good measure of SFR (Krumholz & Tan 2007), rather it should be tracing embedded stellar content. Still, by surveying a sample of massive dense star formation clumps in CS(7–6), CS(2–1), HCN(1–0), and HCN(3–2), Wu et al. (2005, 2010) have extended the relation of L–$L_{\rm HCN(1-0)}$ proposed by Gao & Solomon (2004) down to $L \sim 10^{4.5} L_\odot$ (see Figure 11).

The CHaMP survey provides a way to connect these scales by being a complete census of dense gas and thus star formation activity over a several kpc^2 region of the Galaxy. The CHaMP clumps span the full range of evolution of these sources that will be averaged over in extragalactic observations. In addition, by its improved sensitivity, the CHaMP survey allows us to extend the bolometric-luminosity-versus-dense-gas-line-luminosity relation down to much smaller values of source bolometric luminosity.

In Figure 11 we also plot the CHaMP sources. We fit a power-law relation between L and $L_{\rm HCO^+(1-0)}$ (because of the uncertainties in background subtracted luminosities, we only fit to those sources with $L > 10^{1.5} L_\odot$). Only fitting to the CHaMP clumps (via a least-squares fit in log L) yields

$$\frac{L}{L_\odot} = 917\left(^{+208}_{-170}\right)\left(\frac{L_{\rm HCO^+(1-0)}}{\rm K\ km\ s^{-1} pc^2}\right)^{1.00\pm0.09}. \quad (41)$$

Similarly, a fit to both the CHaMP sample and the extragalactic HCO^+(1–0) of Graciá-Carpio et al. (2006) yields

$$\frac{L}{L_\odot} = 857\left(^{+105}_{-93}\right)\left(\frac{L_{\rm HCO^+(1-0)}}{\rm K\ km\ s^{-1} pc^2}\right)^{1.03\pm0.02}. \quad (42)$$

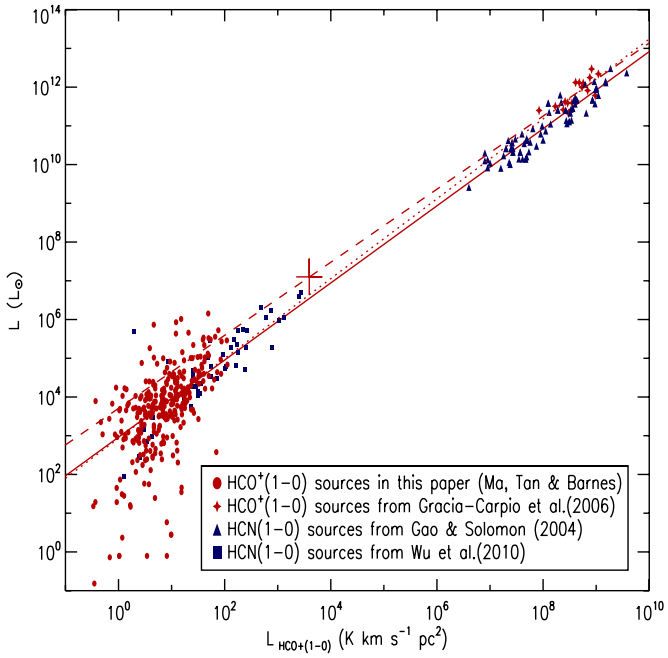

Figure 11. Bolometric luminosity, L, versus dense gas line luminosity, $L_{\mathrm{HCO^+(1-0)}}$. The CHaMP clumps are shown by filled red circles. The single large red cross shows the total luminosity and line luminosity of the whole CHaMP sample. Other $\mathrm{HCO^+}$(1–0) data for entire galaxies from Graciá-Carpio et al. (2006) are shown by red stars. We also show HCN(1–0) data of galactic clumps (Wu et al. (2010)—blue squares) and entire galaxies (Gao & Solomon (2004)—blue triangles). The best-fit relation to only the CHaMP $\mathrm{HCO^+}$(1–0) data (filled red circles) is shown by a solid red line. The best-fit relation to both the CHaMP (filled red circles) and extragalactic $\mathrm{HCO^+}$(1–0) data (red stars) from Graciá-Carpio et al. (2006) is shown by a dotted red line. And the best-fit relation to the total CHaMP data point (red cross) and the extragalactic sample (red stars) is shown by a dashed red line.

(A color version of this figure is available in the online journal.)

Finally, a fit to the total CHaMP data point and the extragalactic sample yields

$$\frac{L}{L_\odot} = 5100\left(^{+6900}_{-2900}\right)\left(\frac{L_{\mathrm{HCO^+(1-0)}}}{\mathrm{K\ km\ s^{-1} pc^2}}\right)^{0.94\pm0.04}. \quad (43)$$

This last fit is expected to be the most accurate for extending current extragalactic results down to lower luminosities. Our results suggest that the L–$L_{\mathrm{HCO^+(1-0)}}$ relation in clumps (when averaged over a complete sample) is almost the same as that found when averaging over whole galaxies.

6. SUMMARY

A total of 303 dense gas clumps have been detected using the $\mathrm{HCO^+}(1-0)$ line in the CHaMP survey (Paper I). In this article we have derived the SED for these clumps using *Spitzer*, *MSX*, and *IRAS* data. By fitting a two-temperature gray-body model to the SED, we have derived the colder component temperature, colder component flux, warmer component temperature, warmer component flux, bolometric temperature, and bolometric flux of these dense clumps. Adopting clump distances and $\mathrm{HCO^+}$-derived masses from Paper I, we have calculated the bolometric luminosities and luminosity-to-mass ratios. These dense clumps typically have masses $\sim$700 $M_\odot$, luminosities $\sim 5\times10^4$ $L_\odot$, and luminosity-to-mass ratios $\sim$70 $L_\odot/M_\odot$.

During the evolution of star-forming clumps, i.e., the formation of star clusters, the luminosity will increase and the gas mass will decrease due to incorporation into stars and dispersal by feedback, causing the luminosity-to-mass ratio to increase. So L/M should be a good evolutionary indicator of the star cluster formation process. The observed range of L/M from $\sim$0.1 $L_\odot/M_\odot$ to $\sim$1000 $L_\odot/M_\odot$ corresponds to that expected for the evolution from starless clumps to those with near equal mass of stars and gas.

The fraction of the warmer component flux in the bolometric flux, F_w/F, has a positive correlation with the luminosity-to-mass ratio, supporting the idea that as stars form in molecular clumps and L/M increases, a larger fraction of the bolometric flux will come out at shorter wavelengths. We also find that the colder component dust temperature, T_c, has a positive correlation with L/M: the bulk of the clump material appears to be getting warmer as the star cluster formation proceeds. However, we caution that our measurements of T_c are relatively poor (they will be improved with the acquisition of *Herschel* observations in this region of the Galaxy). We also find a highly significant correlation of specific intensity in the *Spitzer*-IRAC bands (3–8 μm), I_{IRAC} with L/M. This has the potential to be a useful evolutionary indicator for the star cluster formation process.

We investigated the dependence of L/M with mass surface density, Σ; velocity dispersion, σ; and virial parameter, α_{vir}. The lower limit of the distribution of L/M with Σ is consistent with a model for accretion luminosity powered by accretion rates that are a few percent of the global clump free-fall collapse rate. We do not see strong trends of L/M with Σ and, if present, real effects may be masked by the intrinsic correlation of these variables via M. Similarly, we do not find strong correlations between L/M and σ or α_{vir}.

The bolometric luminosity has a nearly linear correlation with the dense gas mass as traced by $\mathrm{HCO^+}(1-0)$ line luminosity, and this relation holds for over 10 orders of magnitude from molecular clumps in the Milky Way to infrared ultraluminous infrared galaxies. Our results have extended the previously observed relation of Wu et al. (2010) (via HCN(1−0) line observation) down to much lower luminosity clumps. The complete nature of our sample also gives a measurement at intermediate scales ($\sim$several kpc^2) that connects the individual clump results with the extragalactic results, which are averages over clump populations.

J.C.T. acknowledges support from NSF CAREER grant AST-0645412; NASA Astrophysics Theory and Fundamental Physics grant ATP09-0094; and the NASA Astrophysics Data Analysis Program ADAP10-0110. P.J.B. thanks Lisa Torlina and George Papadopoulos at the University of Sydney for their work on an earlier version of this project.

Facilities: IRAS, MSX, Spitzer (IRAC), Mopra (MOPS)

REFERENCES

Aumann, H. H., Fowler, J. W., & Melnyk, M. 1990, AJ, 99, 1674
Barnes, P. J., Ryder, S. D., O'Dougherty, S. N., et al. 2013, MNRAS, 432, 2231
Barnes, P. J., Yonekura, Y., Fukui, Y., et al. 2011, ApJS, 196, 12
Barnes, P. J., Yonekura, Y., Ryder, S. D., et al. 2010, MNRAS, 402, 73
Bertoldi, F., & McKee, C. F. 1992, ApJ, 395, 140
Beuther, H., Schilke, P., Menten, K. M., et al. 2002, ApJ, 566, 945
Egan, M. P., & Price, S. D. 1996, AJ, 112, 2862
Elmegreen, B. G. 2000, ApJ, 530, 277
Elmegreen, B. G. 2007, ApJ, 668, 1064
Faúndez, S., Bronfman, L., Garay, G., et al. 2004, A&A, 426, 97
Gao, Y., & Solomon, P. M. 2004, ApJ, 606, 271
Graciá-Carpio, J., García-Burillo, S., Planesas, P., & Colina, L. 2006, ApJL, 640, L135
Gutermuth, R. A., Megeath, S. T., Myers, P. C., et al. 2009, ApJS, 184, 18

Hennebelle, P., & Falgarone, E. 2012, A&ARv, 20, 55
Hildebrand, R. H. 1983, QJRAS, 24, 267
Hill, T., Burton, M. G., Minier, V., et al. 2005, MNRAS, 363, 405
Hunter, T. R., Churchwell, E., Watson, C., et al. 2000, AJ, 119, 2711
Juneau, S., Narayanan, D. T., Moustakas, J., et al. 2009, ApJ, 707, 1217
Kelly, B. C. 2007, ApJ, 665, 1489
Krumholz, M. R., & Tan, J. C. 2007, ApJ, 654, 304
Lada, C. J., & Lada, E. A. 2003, ARA&A, 41, 57
Ladd, E. F., Adams, F. C., Casey, S., et al. 1991, ApJ, 366, 203
Leitherer, C., Schaerer, D., Goldader, J. D., et al. 1999, ApJS, 123, 3
Li, A., & Draine, B. T. 2001, ApJ, 554, 778
McKee, C. F., & Ostriker, E. C. 2007, ARA&A, 45, 565
McKee, C. F., & Tan, J. C. 2003, ApJ, 585, 850
Molinari, S., Brand, J., Cesaroni, R., & Palla, F. 2000, A&A, 355, 617
Molinari, S., Pezzuto, S., Cesaroni, R., et al. 2008, A&A, 481, 345
Molinari, S., Swinyard, B., Bally, J., et al. 2010, A&A, 518, 100
Mueller, K. E., Shirley, Y. L., Evans, N. J., II., & Jacobson, H. R. 2002, ApJS, 143, 469
Myers, P. C., Adams, F. C., Chen, H., & Schaff, E. 1998, ApJ, 492, 703
Myers, P. C., & Ladd, E. F. 1993, ApJL, 413, L47
Nakano, T., Hasegawa, T., Morino, J.-I., & Yamashita, T. 2000, ApJ, 534, 976
Ossenkopf, V., & Henning, T. 1994, A&A, 291, 943
Palla, F., & Stahler, S. W. 1992, ApJ, 392, 667
Pillai, T., Wyrowski, F., Carey, S. J., & Menten, K. M. 2006, A&A, 450, 569
Roman-Duval, J., Jackson, J. M., Heyer, M., Rathborne, J., & Simon, R. 2010, ApJ, 723, 492
Schaller, G., Schaerer, D., Meynet, G., & Maeder, A. 1992, A&AS, 96, 269
Schnee, S., Enoch, M., Noriega-Crespo, A., et al. 2010, ApJ, 708, 127
Sridharan, T. K., Beuther, H., Schilke, P., Menten, K. M., & Wyrowski, F. 2002, ApJ, 566, 931
Stahler, S. W. 1988, ApJ, 332, 804
Tan, J. C., Krumholz, M. R., & McKee, C. F. 2006, ApJL, 641, L121
Tan, J. C., & McKee, C. F. 2002, in ASP Conf. Ser. 267, Hot Star Workshop III: The Earliest Phases of Massive Star Birth, ed. P. Crowther (San Francisco, CA: ASP), 267
Tan, J. C., Shaske, S. N., & Van Loo, S. 2013, in IAU Symp. 292, Molecular Gas, Dust, and Star Formation, ed. T. Wong & J. Ott (Cambridge: Cambridge Univ. Press), 19
Whittet, D. C. B. 1992, Dust in the Galactic Environment (Bristol: Institute of Physics Publishing), 306
Wu, J., Evans, N. J., II, Gao, Y., et al. 2005, ApJL, 635, L173
Wu, J., Evans, N. J., Shirley, Y. L., & Knez, C. 2010, ApJS, 188, 313
Yonekura, Y., Asayama, S., Kimura, K., et al. 2005, ApJ, 634, 476